Research paper

Experimental constraints on the partitioning of Ru, Rh, Ir, Pt and Pd between chromite and silicate melt: The importance of ferric iron

James M. Brenan [a,*], Craig F. Finnigan [a,b], William F. McDonough [c], Veronika Homolova [a,d]

[a] Department of Geology, University of Toronto, Toronto, Canada
[b] Kaminak Gold, Ltd., Vancouver, Canada
[c] Department of Geology, University of Maryland, College Park, USA
[d] Department of Earth and Environmental Science, Rensselaer Polytechnic Institute, Troy, USA

ABSTRACT

We have performed partitioning experiments to assess the role of chromium-rich spinel in controlling the behavior of the platinum-group elements (PGEs) during igneous differentiation. Spinels were equilibrated with natural and synthetic iron-bearing basalt at 0.1 MPa and 2 GPa at 1400–1900 °C over an fO_2 range of IW + 1.6 to IW + 7.

Results from relatively reduced, graphite-encapsulated experiments done at 2 GPa indicate that Ru is compatible in Cr-spinel (mineral/melt partition coefficient, D, of ~4), followed by Rh and Ir, which are moderately incompatible (D range of 0.04 to ~1), with Pt and Pd the most incompatible (D<0.2). Partition coefficients for Ir, Ru and Rh measured at more oxidizing conditions in this and previous studies are 10 to 1000 times higher than results from experiments using graphite capsules.

We account for the variation in spinel–melt partitioning with a model which considers both the affinity of the PGE cation for a particular spinel lattice site, and the change in site occupancy accompanying the increase in ferric iron component with fO_2. Assuming that Ir and Rh are present as divalent species, with a strong affinity for VI-fold coordination, D_{Ir} and D_{Rh} are predicted to rise rapidly with the ferric iron component, explaining the large D-values for magnetite-rich spinels. Model results indicate that $D_{Ir} \leq 20$ and D_{Rh} are ≤ 100 for ferric-iron poor, Cr-rich compositions, as would crystallize in komatiites, some layered intrusions, and ophiolites. The overall compatibility of Ru for chromite is consistent with the predominance of Ru^{3+} at experiment conditions and the similarity in the size of Ru^{3+} to Cr^{3+} and Fe^{3+}. The increase in D_{Ru} with the ferric iron content of the spinel likely involves a strong effect of mineral composition superimposed on a change in melt speciation (Ru^{2+} to Ru^{3+}) with increased fO_2. The effect of mineral composition is a consequence of the difference in octahedral site preference energy (OSPE) between Ru^{3+}, Fe^{3+} and Cr^{3+}, with stronger partitioning of Ru into Fe^{3+}-rich compositions due to the enhanced reduction in energy gained by the Ru^{3+} substitution. Ru partition coefficients for ferric-iron poor spinel are expected to be ~30, which is somewhat lower than values estimated from natural samples obtained from in situ chromite analyses.

Results indicate that the ferric iron content of chromite exerts a strong control on the partitioning of some PGEs which should be taken into account in both future experimental work and in models of igneous differentiation.

© 2011 Elsevier B.V. All rights reserved.

1. Introduction

There is a longstanding interest in the geochemistry of platinum-group elements (PGEs), particularly in the context of planetary differentiation processes and ore formation. Despite extensive study over the past several decades, the mechanisms by which these elements are concentrated, and fractionated from each other, are still poorly understood. The mineral chromite has been proposed as playing an important role in affecting PGE behavior during melting

and solidification, although evidence for this in natural samples is conflicting. Empirical chromite–silicate melt partition coefficients (Ds or D-values) based on mineral separates and estimates of coexisting melt suggest that Os, Ru and Ir are highly compatible in Cr-bearing spinel, with calculated Ds of up to 150 (Hart and Ravizza, 1996; Puchtel and Humayen, 2001), while Pt and Pd are moderately compatible (D = 1.6–3.3; Puchtel and Humayen, 2001). These observations are consistent with the results of Mitchell and Keays (1981) who identified Cr-spinel, in addition to interstitial sulfide, as the significant PGE-bearing phase in ultramafic xenoliths from various localities. Compatibility of Ir in Cr-rich spinel is also suggested by the correlation between Ir and Cr in various members of the Fiskenaesset Complex (West Greenland; Morgan et al., 1976), and mafic/ultramafic

* Corresponding author.
E-mail address: brenan@geology.utoronto.ca (J.M. Brenan).

lavas (Hamlyn et al., 1985; Crocket and MacRae, 1986; Brugmann et al., 1987), as summarized by Peach and Mathez (1996). Similarly, the compatibility of Ru in chromite from komatiites is also supported by Ru-Cr whole-rock trends (Fiorentini et al., 2008). In addition, cumulate chromitites from layered intrusions, ophiolites, and alpine-type peridotites are known for their anomalously elevated PGE levels (McLaren and DeVilliers, 1982; Page et al., 1982; Talkington and Lipin, 1986, Peck and Keays, 1990; Peck et al., 1992; Von Gruenewaldt and Merkle, 1995, Zhou et al., 1998). Although in some cases, such elevated abundances can be correlated with the presence of discrete PGE-bearing phases (e.g., Legendre and Augé, 1986), detailed high resolution imaging studies have revealed a homogeneous distribution of these elements in chromite from some localities (i.e., Lherz; Ferraris and Lorand, 2008). Other studies, however, have cast some doubt on the importance of chromite as a significant PGE host. Lorand et al. (1998) determined the PGE concentrations in a suite of orogenic lherzolites from the North Pyrenean Metamorphic zone, and found no correlation between PGE content and Cr-spinel abundance. There was, however, a systematic positive correlation between PGE and *sulfur* content, reflecting the control of accessory sulfide minerals. With the exception of a weak trend in the Upper Critical Zone, Maier and Barnes (1999) found no systematic correlation between whole-rock Cr and PGE contents in rocks from the Western Bushveld Complex, consistent with similar observations made for chromite-bearing rocks in ophiolites (e.g., Bacuta et al., 1990; Yang et al., 1995; Zhou et al., 1998). On the basis of whole rock Cr-PGE systematics from komatiitic cumulates, Barnes and Fiorentini (2008) also concluded that there is no significant compatibility of Ir and Rh in chromite. Results of in situ laser ablation ICP–MS (LA–ICP–MS) analyses of chromites from the Merensky Reef (Bushveld Complex) reported by Ballhaus and Sylvestor (2000) indicate less than ~10 ppb PGEs in this phase, whereas Godel et al. (2007) showed that bulk-rock PGE abundances (ppm levels) could be adequately accommodated in trace platinum group minerals. More recently, Pagé et al. (in press) report LA–ICP–MS analyses of chromites from podiform and crustal stratiform chromitites, with results indicating that chromite controls less than 20% of the whole-rock Ir and Ru budgets. However, these workers also found that chromite from the Alexo komatiite contained 450 ppb Ru, thus accounting for the full whole-rock inventory of this element. Locmelis et al. (2011) report similarly elevated Ru concentrations from in situ analyses of chromite from komatiite and komatiitic basalt, but undetectable amounts of the other PGEs.

In contrast to the complexity posed by natural samples, laboratory partitioning studies have consistently shown that spinel-structured minerals may selectively concentrate some PGEs. In terms of partitioning at trace abundance levels, Capobianco and Drake (1990) and Capobianco et al. (1994) measured spinel- and magnetite-silicate melt partition coefficients for Rh, Ru and Pd at 0.1 MPa, 1250–1450 °C and relatively high oxygen fugacities (i.e., FMQ + 1 to FMQ + 7), with their work revealing large partition coefficients for Ru (~20 to >4000) and Rh (~80–300), and uniformly low values for Pd (i.e., <1). These results have been confirmed for Cr-bearing spinel at similar conditions in the more recent work of Righter et al. (2004), who also report a D-value for Ir of 5 to >10,000. In addition to the partitioning experiments, Righter and Downs (2001) showed that magnesioferrite-rich spinels can dissolve wt.% levels of Re, Ru, Ir, Os and Rh, when saturated in the component oxides. Such studies provide an essential part of the framework for understanding the PGE-spinel association, but additional information is required before laboratory results are fully applicable to interpreting natural samples. Of particular importance is the role of ferric iron. Although experiments involving Fe-bearing spinels are clearly relevant to natural igneous suites, nearly all past measurements have produced ferric-iron-rich spinel compositions, owing to the unusually high fO_2 needed to dissolve appreciable PGEs in the melt and spinel phases. Since the presence of ferric iron will have an influence on the uptake of divalent transition metals in VI-fold coordination (see below), the partitioning of some PGEs may also be affected. In the work reported

here, we document partitioning of Ir, Rh and Ru (with limited results for Pt and Pd) for spinel compositions in which Fe^{3+} is nearly completely replaced by Cr^{3+} (and minor Al), and combine these data with past results to provide a framework to understand the role of ferric iron in controlling the uptake of PGEs into the structure of natural, Cr-rich spinels. Before describing the experiments and their results, we briefly review some relevant aspects of site occupancy in chromite–magnetite solid solutions, and their implications for incorporation of the PGEs.

2. Spinel structure and PGE affinity

The structural formula for spinel can be written as $(A_{1-x}B_x)[A_xB_{2-x}]O_4$ in which A and B are di- and trivalent cations (so-called 2,3 spinel) or di- and tetravalent cations (so-called 2,4 spinel) in IV-fold (curved brackets) or VI-fold (square brackets) coordination, and x is the inversion parameter (the reader is referred to Table 1 for a summary of term definitions). The inversion parameter ranges from 0, corresponding to fully "normal" spinel, to 1, or fully "inverted" spinel, in which half of the octahedral sites are occupied by divalent cations. Whereas natural, Cr-rich spinels contain Mg, Al and Ti, for the purpose of illustration, we limit our discussion here to Fe–Cr compositions. Chromite ($FeCr_2O_4$) is a normal spinel, with all Cr in VI-fold coordination owing to the very high octahedral site preference energy (OSPE) of Cr^{3+} (d^3 valence electron configuration; Dunitz and Orgel, 1957; McClure, 1957). In contrast, magnetite (Fe_3O_4) is an inverse spinel at room temperature, but can show some reduction in the amount of divalent octahedral substitution at high temperature (e.g., Wißmann et al., 1998). A general formula for magnetite–chromite solid solutions takes the form:

$(Fe^{2+}_{1-x}Fe^{3+}_x)[Fe^{2+}_xFe^{3+}_{2-2z-x}Cr_{2z}]O_4$, where $Z = Cr^{3+}/(Fe^{3+} + Cr^{3+})$. Kurepin (2005) developed a simple expression for the cation site occupancies in magnetite–chromite solid solutions, accounting for the strong Fe^{2+}–Cr^{3+} interaction on the octahedral sublattice. We have used that expression to calculated the site occupancies across the chromite–magnetite join at representative magmatic conditions of 1300 °C, with results displayed in Fig. 1. For endmember chromite, the octahedral site is completely filled by trivalent cations (Cr^{3+}), thereby restricting the uptake of divalent cations which prefer VI-fold coordination. As the magnetite component increases, however, there is a rise in the divalent cation occupancy of the octahedral site. We note that high temperature site occupancies are similar across the $MgFe_2O_4$–Fe_3O_4 join (Nell et al., 1989), so we expect that either ferric iron component will affect similarly the divalent site occupancy in chromite. With knowledge of charge and octahedral site affinity, it is therefore possible to make some

Table 1
Definition of selected terms used in this study.

| Term	Definition
D	Mineral/melt partition coefficient (wt.% ratio)
D^{2+}_{molar}	Mineral/melt partition coefficient for divalent cations (mole% ratio)
D^{3+}_{molar}	Mineral/melt partition coefficient for trivalent cations (mole% ratio)
x	Spinel inversion parameter; defines the proportion of IV- or VI-fold sites with 2+ and 3+ cations
c^{2+}_{tet}	Concentration of divalent PGE cations in IV-fold coordination
c^{2+}_{oct}	Concentration of divalent PGE cations in VI-fold coordination
y^{2+}_{tet}	Fraction of divalent cation sites in VI-coordination
y^{2+}_{oct}	Fraction of divalent cation sites in IV-coordination
y^{3+}_{tet}	Fraction of trivalent cation sites in VI-coordination
y^{3+}_{oct}	Fraction of trivalent cation sites in IV-coordination
c^{2+}_{melt}	Concentration of divalent PGE cations in the silicate melt
c^{3+}_{melt}	Concentration of trivalent PGE cations in the silicate melt
k^{2+}_{tet}	Divalent cation affinity for IV-coordinated sites
k^{2+}_{oct}	Divalent cation affinity for VI-coordinated sites
k^{3+}_{tet}	Trivalent cation affinity for IV-coordinated sites
k^{3+}_{oct}	Trivalent cation affinity for VI-coordinated sites
$c^{2+}_{tot,spinel}$	Total concentration of divalent PGEs in spinel
$c^{3+}_{tot,spinel}$	Total concentration of trivalent PGEs in spinel
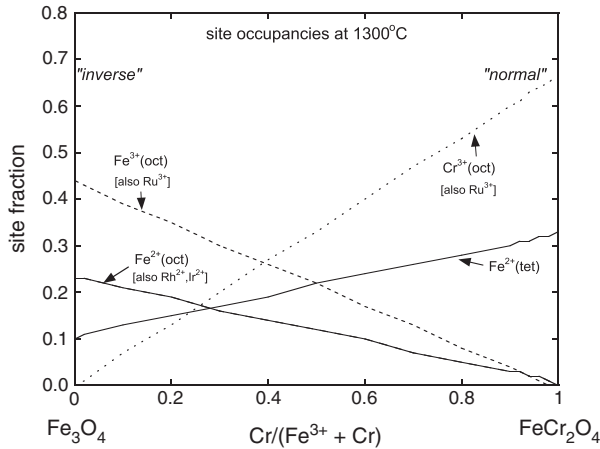
Fig. 1. Variation in the tetrahedral and octahedral site occupancies for di- and trivalent cations across the magnetite–chromite join. Curves are labeled according to the identity of the cation and the site occupied, e.g., Fe^{3+}(oct) refers to the fraction of trivalent iron in VI-fold coordination. Note that the curve for Fe^{2+}(oct) also corresponds to the amount of Fe^{3+} in tetrahedral coordination. All of the Cr^{3+} is assumed to be in VI-fold coordination. Values of the inversion parameter, x (see text and Table 1) calculated at 1300 °C after the method of Kurepin (2005). The species Ru^{3+}, Rh^{2+} and Ir^{2+} are likely to have strong affinity for octahedral coordination, so their substitution into spinel will be controlled by the proportion of di- and trivalent octahedral sites. Consequently, endmember chromite can accommodate Ru^{3+}, but only with increased magnetite component are divalent octahedral sites available for Rh^{2+} and Ir^{2+}.

first-order predictions of the partitioning of PGEs into chromite, and the effect of ferric iron substitution.

Of the PGEs investigated in this study, Rh and Ir are likely to be dissolved as divalent species in oxide solutions at the fO₂ of terrestrial magmas (Borisov and Palme, 1995; O'Neill et al., 1995; Ertel et al., 1999; Brenan et al., 2005), with a d^7 valence electron configuration and in the low spin state (e.g., Zhang et al., 2010). Based on trends in cation size with charge in VI-fold coordination, Rh^{2+} and Ir^{2+} are estimated to have ionic radii of ~72 and 74 pm, respectively, similar to Fe^{2+} and Mg^{2+} (78 and 72 pm, respectively; Shannon and Prewitt, 1969, 1970). Both PGE cations are therefore expected to have a high affinity for octahedral sites in the chromite structure, and owing to their divalent charge, incorporation of Rh and Ir into chromite is predicted to be sensitive to the degree of inversion, as influenced by the magnetite component. Ruthenium is likely dissolved as a trivalent species in oxide solutions at moderate to high fO₂ (Borisov and Nachtweyh, 1998; but see below), with a d^5 electron configuration, also in low spin state (Geschwind and Remeika, 1962), suggesting a strong affinity for octahedral coordination. Based on trends in cation size with charge in VI-fold coordination, Ru^{3+} is estimated to have an ionic radius of ~68 pm, similar to Fe^{3+} and Cr^{3+} (64.5 and 61.5 pm, respectively; Shannon and Prewitt, 1969, 1970). From these considerations, we predict that Ru will be more strongly incorporated into endmember chromite than either Rh or Ir, and that partitioning may change as the magnetite component increases, owing to decreased abundance of trivalent octahedral sites (Fig. 1). The partitioning behavior of Pt and Pd was also considered in this study, and owing to either steric effects (Pt) or charge and size mismatch (Pd), these elements are excluded from the chromite lattice, as discussed later.

3. Experimental techniques

In order to test some of the aforementioned predictions, our goal was to measure chromite–melt partitioning of PGEs in experiments done at low fO₂, in which the magnetite component in chromite is low or absent. We also sought to augment those results with a limited

number of experiments at higher fO₂, so as to assess the effect of magnetite substitution, and compare with previous determinations. A fundamental difficulty of these experiments is the very low solubility of the PGEs in molten or solid oxide at the relatively reduced conditions required to produce ferric-iron free chromite. Although the solubility of PGEs is high at elevated fO₂, the resultant spinel is rich in the magnetite component. It has been determined, however, that PGE solubility is enhanced at higher temperature (cf. Brenan and McDonough, 2009 and references therein) so we have taken advantage of this effect and measured partitioning in experiments done at low fO₂, but temperatures at which the PGEs are measurably soluble in run-product phases. The melt employed in this study is a Tertiary-age microporphyritic alkali olivine basalt from East Greenland (Hogg et al., 1989). This material was first finely powdered in a chrome-steel swing mill to a grain-size of <20 μm, then calcined at 1000 °C in air for 12 h. So as to vary the FeO content of some experiments, we also prepared a synthetic equivalent of this material by weighing oxides and carbonates, grinding the mixture under ethanol, calcining at 1000 °C for 12 h, then subsequent grinding, and drying. We added chromite to experiments as a sieved powder (35–40 or 75–90 μm) prepared by grinding crystals separated from a massive chromitite sample from New Caledonia (Royal Ontario Museum reference # M36331; hereafter N-C chromite). This material was selected as it is chemically homogeneous, mineralogically-pure, free of alteration, and available in relatively large amounts. The PGEs are present at or below detection (by LA–ICP-MS), and we have not observed any platinum group mineral inclusions.

Samples run in high pressure experiments consisted of a basalt: chromite mixture (~2:1 by mass) plus PGE metal, encapsulated in either high purity graphite or Ir doped with small amounts of Fe. Ir–Fe capsules were fabricated from pressed then sintered metal powder mixtures (compositions provided in Table 2). Graphite capsules impose relatively reducing conditions, so higher fO₂ was achieved using the Ir–Fe capsules, which employed melts with high FeO contents and low levels of Fe in the capsule alloy. In graphite-encapsulated experiments, the PGEs were added as a bead of the pure metal (Pt, Rh), a metal mixture (Pd–Ir) or encapsulated in Au (Ru, Ir). The latter material was produced by mixing powders of Au with Ru or Ir then heating in a graphite cup at 1100 °C for ~1 min. This process melts the Au (Tₘ = 1064 °C) causing it to coat the unmelted Ru or Ir grains (Tₘ>2200 °C), resulting in a spherical bead of Au with encapsulated Ru or Ir. Preferential wetting of the Ru or Ir grains by Au texturally isolates them from the silicate melt, which we believe inhibits Ru or Ir nugget formation. A bead of Au was also added to samples encapsulated in Ir–Fe alloy. High pressure experiments were done using a piston-cylinder apparatus employing a 1.27 cm bore pressure vessel with pressure cells consisting of sintered MgO filler pieces and a graphite furnace fit into sleeves of soft-sintered barium carbonate. Samples were subject to 2 GPa confining pressure, and temperatures ranging from 1600 to 1900 °C, with corresponding run durations of 24 h to 100 min. Experiments were terminated by cutting the power to the furnace.

We also report on the results of experiments which were done at 1400–1500 °C and 0.1 MPa using a vertical tube furnace modified for control of fO₂ by gas mixing. Experiment temperatures were monitored using a ceramic-sheathed Pt-Pt10%Rh thermocouple calibrated against the melting point of gold. Oxygen fugacity was fixed by flushing the furnace with pure CO₂, confirmed before and after each experiment using a Y-doped zirconia oxygen probe (Australian Oxytrol Systems, Ltd). Samples were made from a mixture of the natural or synthetic Greenland basalt and sieved N-C chromite which was then combined with polyvinyl alcohol, then bonded to a wire loop and hung from the end of a fused silica rod. Experiments involving Ir, Pt or Rh used loops made from the pure metal (Ir) or metal alloy (Pt/Rh), whereas experiment Ru/Pd-2.5 used pure Pd wire with a bead of Ru inserted into the basalt–chromite mixture. Since Pd is largely immiscible with Ru (~10 wt.% of Pd dissolves in Ru at 1400 °C, and vice versa) high activity

Table 2
Summary of experiments.

Expt ID	T	Duration (h)	Metal	ΔIW[1]	Capsule
HTChr2	1900	1.7	Rh	–	Graphite
HTChr3	1900	1.7	Ru–Au	1.56	Graphite
HTChr4	1800	3.0	Ru–Au	1.60	Graphite
HTChr8	1750	6.0	Rh	–	Graphite
HTChr9	1900	1.7	Rh	–	Graphite
HTChr10	1900	1.7	Ir–Au	1.68	Graphite
HTChr19	1800	3.0	Ir–Pd	–	Graphite
HTChr20	1700	12.0	Ir–Pd	–	Graphite
HTChr22	1800	3.2	Pt	–	Graphite
HTChr26	1600	24.0	Ru–Au	2.14	Graphite
HTChr32	1850	2.8	Ir–Au	5.90	Fe_2Ir_{98}
HTChr33	1850	2.8	Ir–Au	2.04	Graphite
HTChr34	1850	2.8	Ir–Au	5.07	Fe_2Ir_{98}
HTChr35	1850	2.8	Ir–Au	3.05	Fe_7Ir_{93}
HTChr36	1750	6.0	Ru–Au	2.13	Graphite
HTChr37	1850	3.0	Ru–Au	2.04	Graphite
HTCHr39	1850	3.0	Ir–Au	5.03	Fe_2Ir_{98}
RuPd-2.5[2]	1400	168.0	Ru–Pd	7.20	Pd loop
PtRh-2.5[2]	1400	168.0	Pt30%Rh	7.20	Pt–Rh loop
JBIrNC-2[2]	1400	168.0	Ir	7.20	Ir loop
JBIrNC-4a[2]	1500	120.0	Ir	6.10	Ir loop
JBIrNC-4b[2]	1500	120.0	Ir	6.10	Ir loop
JBRhNC-1a[2]	1500	120.0	Pt13%Rh	6.10	Pt–Rh loop
JBRhNC-3[2]	1500	120.0	Pt13%Rh	6.10	Pt–Rh loop

Notes: 1) calculated from the concentration of Fe in Au alloy and FeO in silicate melt (see text). 2) Experiment done at 10^5 Pa on wire loop; all other experiments done at 2 GPa in graphite or metal capsules.

of these metals is maintained during an experiment. Experiments were executed by withdrawing the silica rod to the top of the furnace tube, then sealing the furnace and commencing gas flow. After 20–30 min the sample was slowly lowered into the predetermined hot spot, and remained there for several days. The experiment was terminated by removing the bottom furnace seal and plunging the sample into cold water. A summary of all experiment conditions is provided in Table 2.

4. Sample analysis

Run products were mounted in epoxy and polished with 240 grit SiC, followed by 600 grit SiC, then 1-μm diamond. The major element composition of run-product phases was determined using the Cameca SX50 electron microprobe at University of Toronto. Melt analyses were done using an accelerating voltage of 15 kV, a beam current of 10 nA and a 10–30 μm defocused beam to limit glass damage and to average any chemical heterogeneity arising from the growth of quench phases. Chromite and alloy analyses were done using a 20 kV accelerating voltage and a 30 nA focused beam. Standards for melt analyses were natural basalt (Si, Ca, Al, Fe, Mg), bustamite (Mn), albite (Na), titanium oxide (Ti), chromium oxide (Cr), pentlandite (Ni), sanidine (K), apatite (P) and barite (Ba). Standards for spinel were natural chromite (Cr, Al, Mg), hematite (Fe), bustamite (Mn), titanium oxide (Ti), and pentlandite (Ni). Standards for alloy analysis were high-purity metals. Count times were 10–20 s for most elements, but increased to 60 s to obtain precise Fe (alloy) and Mn (melt, chromite) concentrations. Due to proximity of the Mn-kα to the Cr-kβ peak, we conducted wave-length scans across the Mn peak position in the chromite standard to determine the optimal position for the Mn background measurement. Background count rates for Mn were collected on the high wavelength side of the peak, and extrapolated with zero slope. For all analyses raw count rates were converted to concentrations using the ZAF data reduction scheme. Analyses of Au alloy, quenched melt, and chromite are provided in Tables 3–5.

Trace elements were determined using the laser ablation ICP–MS facilities in the Departments of Geology at the University of Maryland and at University of Toronto. Both systems employ a frequency quintupled

Nd:YAG laser operating at 213 nm, coupled to either an Element 2 (ThermoElectron) magnetic sector ICP–MS (Maryland), or a VG PQExcell quadrupole ICP–MS (Toronto) with He flushing the ablation cell to enhance sensitivity (Eggins et al., 1998). Conditions for laser ablation were typically a 10 Hz repetition rate, with 30 and 100 μm spots for chromite and glass, respectively. Analyses were collected in blocks of 20, with the first and last four spectra acquired on the in-house reference material. Factory-supplied time resolved software was utilized for the acquisition of individual analyses. A typical analysis involved 20 s of background acquisition with the ablation cell being flushed with He, followed by laser ablation for 60 s, then at least 60 s of washout. Data reduction was done off-line using either LAMTRACE (Maryland) or the GLITTER version 5.3 software package (Toronto), supplied by Macquarie Research, Ltd. Concentrations were quantified using the in-house reference material JB-sulfide, which is a NiS bead containing 1920 ppm Mn, 247 ppm Pd, 260 ppm Ru, 237 ppm Rh, 315 ppm Ir and 294 ppm Pt. The PGE concentrations in JB-sulfide were previously quantified using the Hoba Group IVB iron meteorite as the external standard (Walker et al., 2008). Ablation yields were corrected by referencing to the known concentration of Mn in both chromite and melt, as determined by electron microprobe analyses. Mn was used as the internal standard as it is partitioned subequally into both chromite and glass, is not lost to the metal phase during an experiment (as is Ni) and can be measured precisely by both electron probe and LA–ICP–MS in the reference material and unknowns. The following isotopes were used to determine element concentrations reported in this study: ^{99}Ru (in Ni-bearing experiments Rh-2.5 and Pd/Ru-2.5), ^{101}Ru, ^{103}Rh, ^{106}Pd, ^{193}Ir, and ^{195}Pt. As a check for interfering isobars, element concentrations were determined using multiple isotopes when possible. We also assessed the mass interference from $^{85}Rh^{16}O+$, $^{85}Sr^{16}O+$, $^{87}Rb^{16}O+$, $^{87}Sr^{16}O+$, $^{90}Zr^{16}O+$, $^{177}Hf^{16}O+$ and $^{179}Hf^{16}O+$ resulting from impurities in the natural Greenland basalt starting material. This was done by producing an analytical "blank" for the PGEs by fusing the Greenland basalt with added NiS in graphite at high pressure. The resultant glass yielded count rates on the masses of interest which were indistinguishable from background, indicating negligible oxide production from the trace impurities. A summary of trace element concentrations and chromite–melt partition coefficients is provided in Tables 4–6.

Table 3
Summary of gold alloy compositions.

Expt ID	wt.%				
	Fe	Ir	Au	Ru	Total
HTchr3	3.06	na	96.55	0.16	99.77
1 − σ	0.11		0.99	0.13	
HTchr4	2.67	na	96.58	0.48	99.72
1 − σ	0.09		0.69	0.23	
HTChr10	2.05	0.32	97.24	na	99.66
1 − σ	0.10	0.22	0.37		
HTChr26	1.35	na	99.32	0.02	100.69
1 − σ	0.07		0.85	0.03	
HTChr 32	0.11	0.69	99.85	na	100.66
1 − σ	0.02	0.31	0.52		
HTChr 33	1.76	0.25	98.49	na	100.52
1 − σ	0.08	0.29	0.59		
HTChr 34	0.14	0.39	99.85	na	100.39
1 − σ	0.03	0.21	0.60		
HTChr 35	0.96	0.49	98.47	na	99.94
1 − σ	0.09	0.17	0.80		
HTChr36	1.51	na	98.55	0.11	100.17
1 − σ	0.12		0.73	0.11	
HTChr37	1.86	na	98.29	0.03	100.19
1 − σ	0.08		0.84	0.05	
HTChr39	0.23	0.27	99.02	na	99.58
1 − σ	0.03	0.14	0.96		

na — not analyzed.

5. Estimation of oxygen fugacity in high pressure experiments

The amount of Fe dissolved in Au coexisting with FeO-bearing molten silicate can be used to calculate the oxygen fugacity using the heterogeneous equilibrium:

$$Fe^{metal} + \frac{1}{2}O_2 = FeO^{silicate} \qquad (1)$$

which has an equilibrium constant (k_{eq}) of the form,

$$k_{eq} = \left(\frac{a_{FeO}^{silicate}}{a_{Fe}^{metal}}\right)(fO_2)^{-\frac{1}{2}} \qquad (2)$$

in which a_i^j is the activity of component i in phase j. Reference to the iron-wüstite (IW) buffer yields the expression,

$$\log fO_2(\Delta IW) = 2 * \log\left(\frac{a_{FeO}^{silicate}}{a_{Fe}^{metal}}\right) \qquad (3)$$

The activity of the Fe components in the metal and silicate phases are defined as,

$$a_{Fe}^{metal} = \gamma_{Fe}^{metal} * X_{Fe}^{metal} \qquad (4)$$

$$a_{FeO}^{silicate} = \gamma_{FeO}^{silicate} * X_{FeO}^{silicate} \qquad (5)$$

where γ_i^j is the activity coefficient and X_i^j is the mole fraction of species i in phase j. We measured less than 0.5 wt.% of other components (Ru, Ir, Si) in the Au metal phase, so it is essentially a binary Au–Fe solid solution. The value of γ_{Fe}^{metal} was calculated assuming an asymmetric Au–Fe solid solution using the interaction parameters calculated by Borisov and Palme (2000) from the primary data summarized in Hultgren et al. (1973). Values of $\gamma_{FeO}^{silicate}$ were calculated using the composition-dependent parameterization of O'Neill and Eggins (2002). Values of ΔIW calculated for Au-bearing experiments are summarized in Table 2.

6. Results and discussion

6.1. Textural observations

Run products from the experiments done at 0.1 MPa consist of glass containing subhedral chromite and small (<0.1 to 10 μm) crystals of PGE metal at the chromite/melt interface (see Fig. 3a of Finnigan et al., 2008). The metal grains are thought to precipitate along the chromite–melt interface in response to local reduction in oxygen fugacity in the melt, which is the result of the preferential uptake by the chromite crystal of Fe^{3+} relative to Fe^{2+} (see details in Finnigan et al., 2008; note that samples PtRh-2.5 and RuPd-2.5 are also described in Finnigan et al., 2008). Calculations suggest that the magnitude of the fO_2 reduction that drives this process is small (i.e., 0.2 to 0.3 log units) such that the PGE content of the glass sampled by the chromite is only 15–20% lower than the "far-field" concentration. Samples returned from high pressure experiments contained sub- to euhedral chromite immersed in quenched melt consisting of a mixture of fine, dendritic oxide and silicate crystals and glass (Fig. 2), and a metal bead. In experiments containing the Au-encapsulated Ir or Ru, the bead consists of texturally homogeneous Ir or Ru grains surrounded by dendritic gold. We observe very small metal grains at the margins of chromite crystals produced in some high pressure experiments (Fig. 2A), which are also inferred by time-resolved LA–ICP–MS analysis (see below).

6.2. Major and minor element equilibrium

Chromites produced in the high pressure experiments show less than 2% relative variation in their major element composition (Cr, Mg, Al, Fe), based on multiple microprobe analyses (Table 5), indicating phase homogeneity. Minor elements (Ti, Mn) also appear to be homogeneous, as reflected by generally good analytical precision (<5% relative), and for Mn, homogeneity is also shown by the stability of the time-resolved LA–ICP–MS signal (see below). There is some compositional variation in chromites from the low pressure experiments, most notably in terms of the rim-to-core replacement of Cr for Fe^{3+} (see Fig. 5 of Finnigan et al., 2008). For this reason, the reported compositions in Table 2 correspond to the average of values measured at the margin of crystals. The preservation of zoning profiles

Table 4
Summary of melt compositions.

Expt ID	wt.%													ppm					From literature (ppm)	Reference
	SiO_2	TiO_2	Al_2O_3	Cr_2O_3	FeO	MgO	CaO	MnO	Na_2O	K_2O	P_2O_5	sum	Fe^{3+}/Fe^{2+}	Ru	Rh	Pd	Ir	Pt		
Greenland basalt	43.49	4.45	6.82	0.129	12.92	14.81	9.99	0.16	1.6	1.18	0.54	99.06								
HTchr2	39.38	3.83	7.89	10.08	9.51	16.96	8.93	0.192	1.30	0.83	0.37	99.32			6.5					
$1-\sigma$	1.77	0.24	0.27	2.15	0.52	0.90	0.50	0.015	0.28	0.28	0.09				0.3					
HTchr3	37.62	3.72	7.30	9.23	10.81	19.42	8.72	0.196	1.39	0.91	0.40	99.78	0.037	0.43					0.13 (Ru)	1
$1-\sigma$	1.87	0.14	0.30	2.05	0.65	0.66	0.52	0.029	0.22	0.17	0.06			0.06						
HTchr4	40.78	3.83	7.02	5.88	11.45	18.76	9.17	0.169	1.32	0.82	0.45	99.70	0.036	0.08					0.06 (Ru)	1
$1-\sigma$	1.11	0.26	0.18	0.90	0.70	0.70	0.28	0.036	0.30	0.21	0.09			0.01						
HTChr8	41.92	3.78	7.14	4.16	11.18	19.32	9.68	0.189	1.42	0.90	0.43	100.18			0.84					
$1-\sigma$	0.83	0.35	0.13	0.51	0.60	0.52	0.47	0.026	0.30	0.21	0.06				0.14					
HTChr9	38.27	3.55	8.12	10.07	11.24	16.56	8.61	0.214	1.46	0.90	0.50	99.55			5.8					
$1-\sigma$	1.26	0.23	0.20	1.89	0.38	0.49	0.32	0.038	0.21	0.17	0.09				1.0					
HTChr10	39.18	3.29	7.16	6.26	5.17	27.86	8.39	0.147	1.30	1.01	0.04	99.83	0.041				0.12		0.1 (Ir)	2
$1-\sigma$	0.83	0.30	0.42	0.95	0.23	1.37	0.89	0.029	0.16	0.17	0.03						0.01			
HTChr19	42.89	3.86	7.60	3.07	2.45	24.67	11.13	0.16	1.08	0.98	0.01	98.32				15	0.033			
$1-\sigma$	1.31	0.59	0.41	0.88	0.20	2.27	2.00	0.03	0.19	0.25	0.01					1	0.004			
HTChr20	44.68	4.07	6.98	3.04	4.87	20.28	11.49	0.15	1.06	1.03	0.02	97.73				4.4	0.016			
$1-\sigma$	0.67	0.42	0.24	0.80	0.33	0.17	0.36	0.07	0.15	0.02						0.6	0.003			
HtChr22	44.89	3.96	7.11	4.42	3.29	24.04	10.06	0.15	0.73	0.73	0.00	99.39						0.90		
$1-\sigma$	0.84	0.33	0.20	0.40	0.14	0.42	0.36	0.02	0.15	0.17	0.00							0.03		
HTChr26	43.95	4.28	7.12	2.15	10.67	16.82	10.90	0.18	1.29	0.90	0.56	98.85	0.045	0.11					0.02 (Ru)	1
$1-\sigma$	0.40	0.23	0.06	0.26	0.49	0.29	0.21	0.02	0.13	0.13	0.11			0.02						
HTChr32	34.36	3.58	7.10	3.32	22.56	15.37	11.45	0.33	1.00	0.44	0.00	99.52	0.242				2.5			
$1-\sigma$	0.97	0.42	0.31	1.42	1.14	1.19	0.99	0.17	0.12								0.1			
HTChr33	40.40	3.73	7.62	5.29	7.19	21.07	12.41	0.23	0.46	0.53	0.00	98.96	0.049				0.12		0.1 (Ir)	2
$1-\sigma$	1.68	0.44	0.48	1.43	0.68	1.74	1.22	0.01	0.04	0.08	0.00						0.03			
HTChr34	40.95	4.15	7.94	2.09	11.85	17.70	13.12	0.24	1.43	0.95	0.03	100.48	0.200				0.73			
$1-\sigma$	0.96	0.23	0.33	0.86	0.69	1.17	0.57	0.04	0.18	0.03							0.04			
HTChr35	35.51	3.28	5.92	2.98	5.13	35.75	11.59	0.17	1.16	0.85	0.04	102.39	0.079				0.10			
$1-\sigma$	0.56	0.60	0.75	0.42	0.32	2.68	1.58	0.03	0.27	0.17	0.03						0.02			
HTChr36	43.32	3.94	7.25	4.43	9.12	18.37	10.27	0.19	1.18	0.89	0.49	99.49	0.047	0.036					0.08 (Ru)	1
$1-\sigma$	0.88	0.19	0.15	0.40	0.41	0.46	0.26	0.02	0.14	0.15	0.08			0.003						
HTChr37	41.96	3.87	7.73	7.34	9.50	17.52	9.75	0.19	1.27	0.72	0.47	100.35	0.046	0.14					0.17 (Ru)	1
$1-\sigma$	0.65	0.22	0.10	0.62	0.29	0.49	0.23	0.02	0.14	0.14	0.07			0.01						
HTChr39	37.40	3.83	8.08	1.89	18.61	17.31	11.05	0.29	0.55	0.58	0.06	99.66	0.162				0.77			
$1-\sigma$	0.32	0.23	0.37	1.30	0.89	0.52	0.25	0.05	0.16	0.22	0.04						0.12			
RuPd-2.5	49.62	4.22	7.4	0.4	12.77	13.84	9.27	0.19	0.88	0.23	0.06	98.88	0.455	2.4		174			10 (Ru); 85 (Pd; higher with FeO)	1, 3, 4
$1-\sigma$	0.31	0.2	0.14	0.04	0.34	0.13	0.11	0.03	0.05	0.02	0.06			0.8		3				
PtRh-2.5	45.69	4.61	7.88	0.30	13.39	14.93	10.13	0.18	0.69	0.16	0.11	98.07	0.457		3.56			0.53	4.5 (Rh); 1 (Pt)	5
$1-\sigma$	0.37	0.15	0.09	0.02	0.32	0.15	0.13	0.03	0.06	0.02	0.05				0.09			0.02		
JBIrNC-2	41.11	3.74	6.95	0.11	18.78	15.63	12.53	0.37	0.58	0.04	0.03	99.86	0.469				0.107		0.08 (Ir)	6
$1-\sigma$	0.22	0.22	0.17	0.04	0.26	0.17	0.12	0.02	0.04	0.02	0.04						0.002			
JBIrNC-4a	42.63	4.53	8.13	0.37	11.91	18.86	13.02	0.24	0.24	0.02	0.02	99.98	0.308				0.151		0.08 (Ir)	6
$1-\sigma$	0.22	0.20	0.06	0.04	0.20	0.14	0.14	0.03	0.03	0.01	0.03						0.004			
JBIrNC-4b	38.18	3.80	6.75	0.29	23.63	15.87	11.60	0.37	0.20	0.02	0.03	100.73	0.267				0.30		0.08 (Ir)	6
$1-\sigma$	0.16	0.18	0.06	0.04	0.24	0.09	0.11	0.03	0.03	0.02	0.03						0.02			
JBRhNC-1a	38.31	3.93	6.82	0.30	22.53	16.11	11.60	0.37	0.12	0.02	0.03	100.13	0.269		1.86			2.15	6.8 (Rh); 1.3 (Pt)	5
$1-\sigma$	0.23	0.19	0.12	0.03	0.24	0.10	0.11	0.03	0.03	0.01	0.04				0.03			0.01		
JBRhNC-3	45.41	4.67	7.67	0.53	14.12	15.05	10.26	0.20	0.43	0.06	0.02	98.44	0.282		1.38			0.89	6.8 (Rh); 1.3 (Pt)	5
$1-\sigma$	0.16	0.16	0.09	0.04	0.28	0.09	0.13	0.03	0.05	0.02	0.03				0.01			0.01		

Notes: a) References for solubility estimates: 1) Borisov and Nachtweyh (1998); 2) Brenan and McDonough (2009); 3) Borisov et al. (1994); 4) Laurenz et al. (2010); 5) Fortenfant et al. (2003); 6) Brenan et al.(2005). b) melt Fe^{3+}/Fe^{2+} calculated by the method of Kress and Carmichael (1991) for experiments in which the fO_2 could be estimated. c) Greenland basalt composition sum includes 1.91 wt.% loss on ignition.

in chromites from low pressure experiments suggests the original sieved grains have partially re-equilibrated by volume diffusion, with limited growth of new chromite grains by dissolution/reprecipitation. Owing to much higher temperatures, and the considerably higher solubility of Cr in melts from the high pressure experiments (>1 wt.% at 2 GPa, vs ≤0.4 wt at 0.1 MPa; Table 4), both volume diffusion and the flux of components during dissolution/reprecipitation were more efficient, resulting in phase homogeneity.

The major element composition of run-product chromites show a significant shift relative to the N-C chromite starting material, particularly in terms of ferric iron content (calculated from stoichiometry after the method of Barnes and Roeder, 2001). Whereas the N-C chromite has $Fe^{3+}/(Fe^{3+}+Cr+Al)$ of ~0.06, some chromites produced in graphite capsules are essentially devoid of Fe^{3+}, and those grown in Ir–Fe alloy or in the gas-mixing furnace overlap and exceed initial values. Values of $Fe^{3+}/(Fe^{3+}+Cr+Al)$ show an exponential increase with oxygen fugacity (Fig. 3), consistent with the expected increase in Fe^{3+}/Fe^{2+} in the melt with more oxidizing conditions. The form of the ferric iron-fO_2 variation exhibited by chromite from our experiments is identical in manner to the reversed experiments of Roeder and Reynolds (1991)(Fig. 3). Although the specific value of $Fe^{3+}/(Fe^{3+}+Cr+Al)$ at a given fO_2 may be different, this likely arises from the effect of melt composition on the speciation of iron (e.g., Kress and Carmichael, 1991).

We have also evaluated the chromite–melt Fe–Mg exchange systematics by calculating the $Fe^{2+}/(Fe^{2+}+Mg)$ in melt and

Table 5
Summary of chromite compositions.

Expt ID	wt.%									Cations p.f.u.			ppm				
	SiO_2	TiO_2	Al_2O_3	Cr_2O_3	FeO	Fe_2O_3[a]	MnO	MgO	Total	Cr	Al	Fe^{3+}	Ru	Rh	Pd	Ir	Pt
NC chromite	–	0.13	10.68	58.63	10.15	5.20	0.150	15.44	100.4	0.737	0.200	0.062					
$1-\sigma$	–	*0.02*	*0.10*	*0.45*	*0.64*	*0.23*	*0.030*	*0.39*									
HTchr2	0.20	0.77	9.30	63.92	10.04	0.00	0.114	15.33	99.7	0.822	0.178	0.000		0.40			
$1-\sigma$	*0.02*	*0.14*	*0.36*	*1.36*	*0.51*	*0.00*	*0.004*	*0.13*						*0.030*			
HTchr3	0.21	0.87	9.57	63.64	9.39	0.00	0.099	16.21	100.0	0.817	0.183	0.000	1.25				
$1-\sigma$	*0.03*	*0.03*	*0.07*	*0.49*	*0.07*	*0.00*	*0.005*	*0.10*					*0.03*				
HTchr4	0.23	1.17	10.33	62.27	11.03	0.28	0.101	15.60	101.0	0.799	0.198	0.003	0.54				
$1-\sigma$	*0.02*	*0.04*	*0.20*	*0.32*	*0.08*	*0.00*	*0.006*	*0.10*					*0.12*				
HTChr8	0.26	1.25	10.45	60.23	10.46	0.75	0.117	15.62	99.1	0.787	0.204	0.009		0.19			
$1-\sigma$	*0.04*	*0.04*	*0.11*	*0.38*	*0.04*	*0.00*	*0.003*	*0.08*						*0.031*			
HTChr9	0.19	0.65	9.46	64.28	10.01	0.00	0.120	15.38	100.1	0.820	0.180	0.000		0.23			
$1-\sigma$	*0.04*	*0.04*	*0.17*	*0.33*	*0.09*	*0.00*	*0.004*	*0.26*						*0.015*			
HTChr10	0.27	0.97	10.95	63.89	3.80	0.00	0.079	19.92	99.9	0.796	0.204	0.000				0.019	
$1-\sigma$	*0.08*	*0.11*	*0.48*	*0.71*	*0.14*	*0.00*	*0.006*	*0.39*								*0.010*	
HTChr19	0.23	0.94	11.54	64.04	2.35	0.00	0.085	20.78	100.0	0.788	0.212	0.000			<0.14	0.010	
$1-\sigma$	*0.03*	*0.06*	*0.29*	*0.48*	*0.04*	*0.00*	*0.006*	*0.14*								*0.002*	
HTChr20	0.35	0.92	12.33	61.51	5.87	0.14	0.107	18.80	100.0	0.769	0.230	0.002			<0.16	0.014	
$1-\sigma$	*0.02*	*0.02*	*0.05*	*0.24*	*0.06*	*0.00*	*0.004*	*0.07*								*0.003*	
HtChr22	0.28	1.08	10.63	63.72	3.48	0.14	0.105	20.22	99.64	0.799	0.199	0.002					<0.023
$1-\sigma$	*0.02*	*0.04*	*0.21*	*0.38*	*0.04*	*0.00*	*0.006*	*0.10*									
HTChr26	0.24	1.48	10.59	59.49	11.51	1.47	0.124	15.30	100.05	0.776	0.206	0.018	0.34				
$1-\sigma$	*0.01*	*0.02*	*0.09*	*0.31*	*0.05*	*0.01*	*0.007*	*0.10*					*0.1*				
HTChr 32	0.23	0.72	8.57	54.53	11.83	9.61	0.174	14.26	98.96	0.713	0.167	0.120				33	
$1-\sigma$	*0.01*	*0.03*	*0.07*	*0.25*	*0.06*	*0.05*	*0.007*	*0.05*								*2*	
HTChr 33	0.26	1.02	11.13	61.29	6.69	0.31	0.133	18.01	98.88	0.786	0.211	0.004				0.021	
$1-\sigma$	*0.02*	*0.03*	*0.13*	*0.27*	*0.06*	*0.00*	*0.007*	*0.14*								*0.002*	
HTChr 34	0.25	0.62	9.07	60.57	8.49	4.04	0.129	16.46	99.23	0.777	0.174	0.049				1.8	
$1-\sigma$	*0.02*	*0.02*	*0.07*	*0.24*	*0.06*	*0.03*	*0.005*	*0.07*								*0.1*	
HTChr 35	0.22	1.11	11.62	61.10	2.36	1.79	0.069	21.01	99.11	0.762	0.216	0.021				0.40	
$1-\sigma$	*0.12*	*0.27*	*0.17*	*0.93*	*0.03*	*0.02*	*0.005*	*0.25*								*0.02*	
HTChr36	0.24	0.97	9.60	62.06	9.50	0.82	0.110	16.05	99.25	0.804	0.186	0.010	0.18				
$1-\sigma$	*0.01*	*0.03*	*0.11*	*0.20*	*0.09*	*0.01*	*0.003*	*0.08*					*0.1*				
HTChr37	0.23	0.70	8.87	64.04	10.49	0.01	0.110	15.25	99.70	0.829	0.171	0.000	0.43				
$1-\sigma$	*0.01*	*0.02*	*0.07*	*0.35*	*0.06*	*0.00*	*0.004*	*0.09*					*0.13*				
HTChr39	0.21	0.59	8.97	56.64	11.68	7.09	0.254	14.26	98.98	0.738	0.174	0.088				2.9	
$1-\sigma$	*0.01*	*0.03*	*0.08*	*0.22*	*0.08*	*0.05*	*0.008*	*0.13*								*0.9*	
RuPd-2.5	0.06	1.10	5.27	47.03	7.02	23.48	0.230	16.51	100.96	0.619	0.103	0.277	91		5.5		
$1-\sigma$	*0.01*	*0.11*	*0.24*	*1.8*	*0.34*	*1.6*	*0.030*	*0.32*					*9*		*0.5*		
PtRh-2.5	0.06	1.57	6.29	40.33	5.13	28.97	0.250	17.68	100.58	0.534	0.124	0.342		316			<0.06
$1-\sigma$	*0.01*	*0.09*	*0.16*	*1.16*	*0.33*	*0.79*	*0.030*	*0.2*						*63*			
JBIrNC-2	0.13	2.00	7.42	23.89	11.30	39.06	0.34	14.62	98.76	0.331	0.153	0.515				20	
$1-\sigma$	*0.01*	*0.06*	*0.09*	*1.04*	*0.19*	*0.65*	*0.01*	*0.09*								*1*	
JBIrNC-4a	0.07	1.35	9.67	48.29	6.83	14.58	0.22	17.71	98.71	0.631	0.188	0.181				16	
$1-\sigma$	*0.02*	*0.12*	*0.47*	*1.44*	*0.19*	*0.40*	*0.01*	*0.10*								*2*	
JBIrNC-4b	0.10	1.61	7.78	28.80	11.91	33.89	0.30	14.04	98.44	0.396	0.160	0.444				23	
$1-\sigma$	*0.01*	*0.03*	*0.05*	*0.46*	*0.10*	*0.29*	*0.00*	*0.04*								*2*	
JBRhNC-1a	0.10	1.59	8.16	30.14	11.48	32.44	0.31	14.42	98.60	0.412	0.166	0.422		88			<0.2
$1-\sigma$	*0.01*	*0.03*	*0.06*	*0.28*	*0.07*	*0.20*	*0.01*	*0.07*						*6*			
JBRhNC-3	0.06	1.09	6.67	51.28	10.97	14.15	0.21	14.63	99.06	0.687	0.133	0.180		71			<0.2
$1-\sigma$	*0.01*	*0.02*	*0.07*	*0.37*	*0.09*	*0.12*	*0.01*	*0.10*						*3*			

[a] Ferric iron content and cations per formula unit (p.f.u.) calculated after the method of Barnes and Roeder (2001).

chromite, using the formulation of Kress and Carmichael (1991) to apportion the FeO and Fe_2O_3 abundances in run-product melts. Compositions of coexisting chromite and melt produced in our experiments and those of Roeder and Reynolds (1991), are portrayed in Fig. 4. The data of Roeder and Reynolds (1991), which include reversed results, define a linear array projecting through the origin, with a constant ratio of $Fe^{2+}/(Fe^{2+}+Mg)_{chr}/Fe^{2+}/(Fe^{2+}+Mg)_{melt}$ equal to 1.16. Our data overlap this array, consistent with chromite–melt equilibrium in our experiments.

A comparison between the chromite compositions produced in this study with those from previous PGE partitioning experiments, and the range from select cumulate and ultramafic igneous rock suites, is portrayed in Fig. 5. Chromites produced in our experiments have relatively elevated and nearly constant $Cr/(Cr+Al)$ (~0.8), with $Fe^{2+}/(Fe^{2+}+Mg)$ below ~0.4 (Fig. 5A). This value of $Cr/(Cr+Al)$ is at the high end of the range for chromites from natural parageneses, whereas the $Fe^{2+}/(Fe^{2+}+Mg)$ is lower. Righter et al. (2004) produced spinels with $Fe^{2+}/(Fe^{2+}+Mg)$ similar to those from our experiments, but $Cr/(Cr+Al)$ spanning a much larger range, with values extending to Cr-free compositions. Capobianco et al. (1994) produced nearly Mg-free magnetite in their experiments, with both $Cr/(Cr+Al)$ of ~0.5 and Cr-free compositions. The ratio of $Fe^{3+}/(Fe^{3+}+Cr+Al)$ in chromites from natural suites is ~0.3 or lower (Fig. 5B), similar to the span produced in this study, although the majority of our experiments yielded chromites with values less than 0.05. As mentioned above, most previous PGE partitioning experiments produced spinels with rather high Fe^{3+} contents, reflecting the oxidizing conditions imposed on those samples. With the exception of two values of ~0.15 (Righter et al., 2004), most of this past work has produced spinels with $Fe^{3+}/(Fe^{3+}+Cr+Al)$ of >0.5.

6.3. Trace element behavior

6.3.1. Phase homogeneity

Examples of time resolved spectra for run product chromites and glasses are shown in Fig. 6. Quenched melts show a homogeneous

Table 6
Summary of chromite–melt partition coefficients.

Expt ID	Ru	1 − σ	Rh	1 − σ	Pd	1 − σ	Ir	1 − σ	Pt
HTchr3	2.91	0.38							
HTchr4	6.75	1.78							
HTChr26	3.09	1.05							
HTChr36	5.00	2.78							
HTChr37	3.07	0.96							
RuPd-2.5	37.9	13.5			0.032	0.003			
HTchr2			0.062	0.006					
HTChr8			0.226	0.052					
HTChr9			0.040	0.007					
PtRh-2.5			89	18					<0.11
JBRhNC-1a			47	3					<0.09
JBRhNC-3			51	2					<0.22
HTChr10							0.16	0.09	
HTChr19					<0.0093		0.31	0.07	
HTChr20					<0.036		0.88	0.24	
HTChr 32							13.20	0.88	
HTChr 33							0.18	0.04	
HTChr 34							2.47	0.19	
HTChr 35							4.00	0.71	
HTChr39							3.77	1.31	
JBIrNC-2							186.9	10.4	
JBIrNC-4a							106.0	10.1	
JBIrNC-4b							76.7	8.5	
HtChr22									<0.026

distribution of PGEs, in accordance with the uniform count rates for these elements with ablation time (= depth into sample). In general, run-product chromites were also found to be homogeneous, but two distinct types of inhomogeneity were encountered in some experiments. The first type was seen in chromites produced in low pressure experiments, which, as noted above, display some core-to-rim major element zonation. In this case, PGE concentrations in larger grains increase from core to rim, consistent with diffusion from the PGE-rich melt into an initially PGE-free crystal. For the purposes of calculating a partition coefficient, we report the average of values measured for the smallest grains (≤50 μm). The second type of inhomogeneity was found in the products of some high pressure experiments, in which PGE-rich regions occur both in the melt near the crystal–melt boundary, and within some chromite grains. The location of these domains at the crystal–melt boundary was confirmed by the rapid rise in the time-resolved signal for PGE and Ca, indicating the laser had ablated through the chromite (Fig. 6C). Melts from these high pressure experiments were found to be essentially free of PGE inhomogeneity (Fig. 6D). We interpret these PGE-rich regions as arising from small metal grains formed at the chromite margin during crystal growth, which in some cases become trapped as the crystal margin migrates. Finnigan et al. (2008) proposed a mechanism for this process involving local reduction and metal precipitation during crystal growth as a consequence of the selective uptake by chromite of Cr^{3+} relative to Cr^{2+}. This is similar to the mechanism described previously to account for the formation of metal grains in the low pressure experiments, where metal precipitation is a consequence of crystal growth instead of diffusive re-equilibration. We obtained reliable PGE concentrations in chromites from such experiments by careful signal selection during data processing.

6.4. PGE content of run-product melts

A comparison between the PGE content of the melts produced in this study with solubilities determined in previous studies is provided in Table 4, and plotted in Fig. 7. As PGE solubilities change systematically with fO₂, only experiments in which the fO₂ could be estimated are included in this comparison. Although the temperature dependence to the metal solubility can also be estimated from previous results, accounting for differences in melt compositions is not so straightforward. Whereas previous work on Ir and Pd solubility

have used Fe-bearing basaltic compositions (Brenan et al., 2005; Brenan and McDonough, 2009; Laurentz et al., 2010), results for Ru, Rh and Pt have only been determined using the Fe-free diopside–anorthite eutectic composition (Borisov and Nachtweyh, 1998; Fortenfant et al., 2003). As shown by Laurentz et al. (2010), the solubility of Pd increases with melt ferric iron content, but the general extension of this result to other PGEs awaits further experiments. Other compositional parameters, such as the proportion of bridging oxygens (as gaged by the melt SiO₂ and Al₂O₃ content), have also been shown to affect PGE solubility (Borisov and Danyushevsky, 2011). Given these uncertainties, the PGE contents of run-product melts are in reasonable accord with past results, agreeing within a factor of two (median) to five (worst case).

7. Chromite–Melt partition coefficients

A summary of chromite–melt partition coefficients from all experiments is shown in Fig. 8. For graphite-encapsulated samples, D-values show marked differences, with Ru exhibiting compatible behavior (D of ~4), followed by Rh and Ir, which are moderately incompatible (D range of 0.04 to ~1), with Pt and Pd the most incompatible (D<0.2). Whereas the partition coefficients for Ru are relatively invariant with temperature, values for Ir and Rh increase with decreasing T. Partition coefficients measured in experiments done with Ir–Fe capsules are more than 10× higher than values measured for graphite-encapsulated samples run at the same temperature. Similarly, D_{Ru}, D_{Rh} and D_{Ir} measured at 0.1 MPa are ~10× (Ru) to >100× (Rh, Ir) higher than results from experiments using graphite capsules.

As noted in the Introduction, past experiments on spinel–melt partitioning of the PGEs at moderate to high oxygen fugacity have shown that Ru, Rh and Ir are all strongly compatible, with D-values of ~20 to >1000, whereas D_{Pd} is one or less (Capobianco and Drake, 1990; Capobianco et al., 1994; Righter et al., 2004). Although our results suggest stronger incompatibility of Pd in chromite, the relative partitioning of Pd to the other PGEs is consistent with previous work. The more severe discrepancy lies in the much smaller partition coefficients we have measured for Ru, Ir and Rh, in the graphite-encapsulated experiments. In the context of the previous description of spinel structure and PGE affinity, below we discuss reasons for the observed variations in PGE partition coefficients.
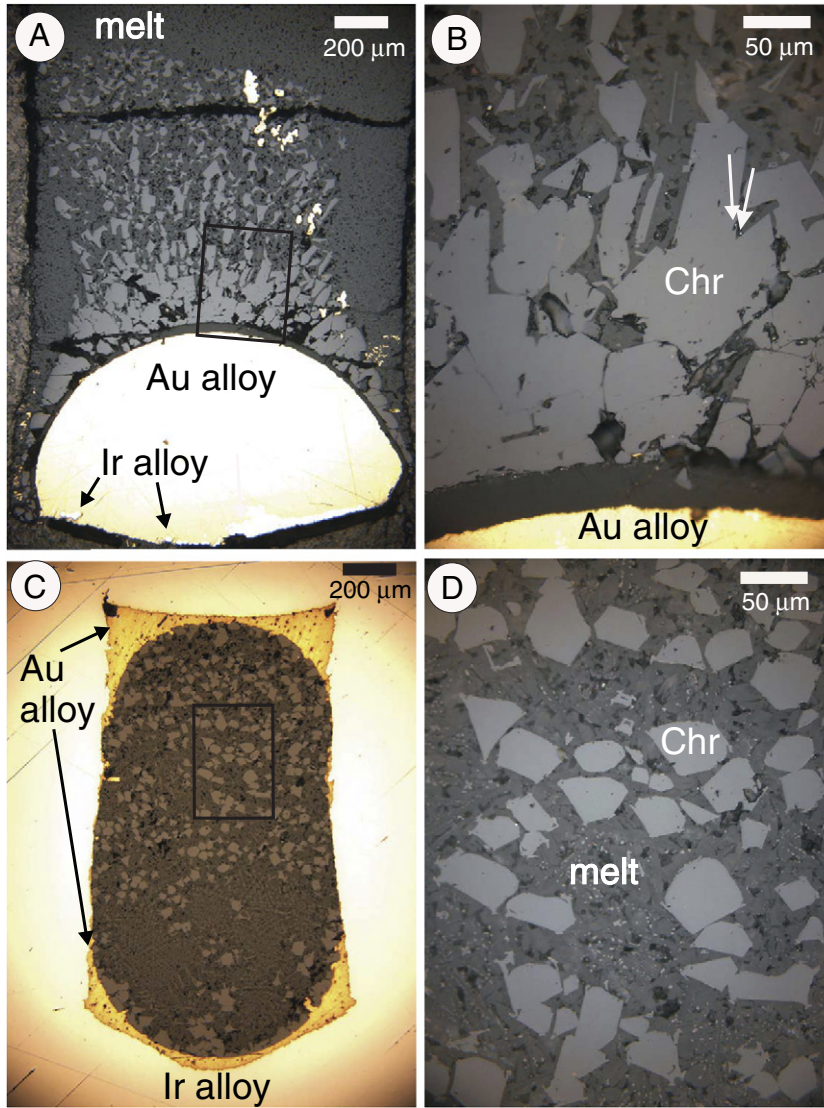
Fig. 2. Reflected light photomicrograph of the sectioned run products from experiments HTChr33 (graphite encapsulated; A, B) and 32 (Ir–Fe alloy encapsulated; C, D), each done at 1850 °C, 2 GPa, for 2.8 h. The field of view in B and D corresponds to the rectangles in A and C, respectively. Chromite, which was added as a finely ground powder, with a grain size less than 40 μm, has dissolved and reprecipitated to form equant crystals. The melt has quenched to a fine intergrowth of silicate and oxide crystals plus glass. Note the preferential wetting of the Ir alloy by Au. White arrows in B point to small metal grains at the chromite–melt interface.

7.1. Rh and Ir partitioning and the role of spinel inversion

Studies suggest that Rh and Ir are dissolved as 2+ cations in oxide solutions over a range of fO_2, and their valence shell electron structure indicates a strong preference for octahedral coordination. Consequently, the availability of VI-fold sites likely influences spinel–melt partitioning of the PGEs. Relative occupancy of divalent PGE cations in IV- or VI-coordination (c^{2+}_{tet} and c^{2+}_{oct}, respectively) is controlled by both the abundance of each spinel site (y^{2+}_{tet} and y^{2+}_{oct}), and the concentration of the divalent cation in the melt (c^{2+}_{melt}):

$$c^{2+}_{tet} = k^{2+}_{tet}\, y^{2+}_{tet}\, c^{2+}_{melt} \qquad (6)$$

$$c^{2+}_{oct} = k^{2+}_{oct}\, y^{2+}_{oct}\, c^{2+}_{melt} \qquad (7)$$

in which k^{2+}_{tet} and k^{2+}_{oct} are constants describing the affinity of each site for the PGE cation. The total concentration of divalent PGE cations in spinel ($C^{2+}_{tot,spinel}$) is therefore expressed as:

$$C^{2+}_{tot,spinel} = \left(k^{2+}_{tet}\, y^{2+}_{tet}\, c^{2+}_{melt}\right) + \left(k^{2+}_{oct}\, y^{2+}_{oct}\, c^{2+}_{melt}\right) \qquad (8)$$

and dividing both sides by c^{2+}_{melt} yields:

$$C^{2+}_{tot,spinel} / c^{2+}_{melt} = \left(k^{2+}_{tet}\, y^{2+}_{tet}\right) + \left(k^{2+}_{oct}\, y^{2+}_{oct}\right) \qquad (9)$$

which is the spinel–melt partition coefficient for divalent cations. Expressed on a molar basis, y^{2+}_{tet} is equal to $(1-x)/3$, and $y^{2+}_{oct} = x/3$. Therefore the molar partition coefficient is expressed as:

$$D^{2+}_{molar} = \left(k^{2+}_{tet}\, ((1-x)/3)\right) + \left(k^{2+}_{oct}\, (x/3)\right). \qquad (10)$$

Eq. (10) predicts that the partition coefficient for divalent cations should increase with the degree of inversion, provided the cation affinity is larger for VI-fold, rather than IV-fold coordination.

We first apply these relations qualitatively to understand the change in D-values for Ir and Rh with decreasing temperature for graphite-encapsulated samples. Chromite produced in those experiments contains variable amounts of both Fe^{3+} and Al, such that $Cr/(Fe^{3+} + Cr + Al)$ decreases with decreasing T (Fig. 9A). The addition of both Fe^{3+}- and Al-bearing components will cause partial inversion of the chromite structure and create divalent VI-fold sites.
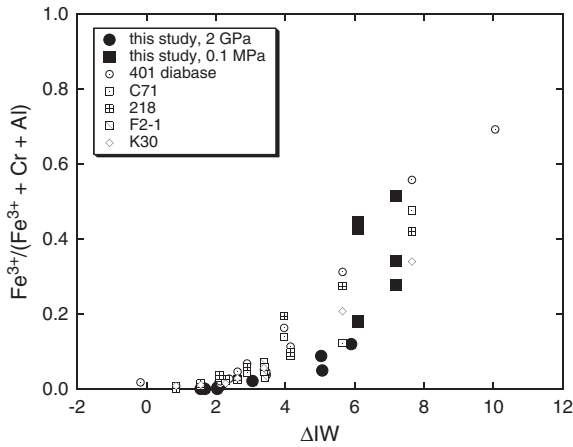
Fig. 3. Variation in the $Fe^{3+}/(Fe^{3+}+Cr+Al)$ of chromite as a function of oxygen fugacity relative to the iron-wüstite buffer. Results are shown from this study and Roeder and Reynolds (1991) who grew chromite from several different melt compositions. The ferric iron content of chromites is calculated from mineral stoichiometry after the method of Barnes and Roeder (2001). The large increase in the ferric iron content of the chromite near $IW+6$ arises from the rapid change in the melt Fe^{3+}/Fe^{2+} over this range of fO_2.

Provided $k^{2+}_{tet} < k^{2+}_{oct}$, this reduction in $Cr/(Fe^{3+}+Cr+Al)$ should correlate with an increase in the chromite–melt partition coefficient, as indicated by the data shown in Fig. 9B. Therefore, the change in partitioning for Ir and Rh observed for graphite-encapsulated experiments may not be due to an intrinsic T dependence to the partitioning, but results from differences in chromite composition. This is also consistent with the results of the Ir partitioning experiments which produced nearly the same chromite compositions ($Cr/(Fe^{3+}+Cr+Al) = 0.790 \pm 0.005$) and similar values of D_{Ir} (~0.2; Fig. 9B) despite being done over a temperature range of 100 °C.

In the above analysis, we assume *a priori* that $k^{2+}_{tet} < k^{2+}_{oct}$, and conclude that partition coefficients should increase with an increased abundance of divalent VI-fold sites. Although this is a reasonable assumption, further evidence for this is in order. PGE incorporation into natural spinels appears to be consistent with this analysis, as Park et al. (2010) have shown positive correlations
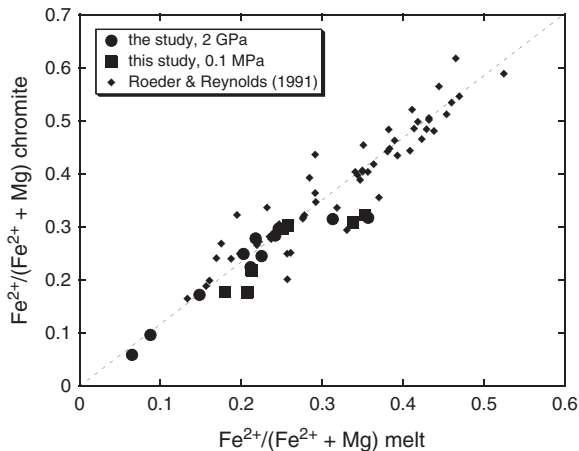
Fig. 4. Variation in the $Fe^{2+}/(Fe^{2+}+Mg)$ in melt and coexisting chromite from the experiments of this study and Roeder and Reynolds (1991). The Fe^{2+} content of chromite is calculated from mineral stoichiometry after the method of Barnes and Roeder (2001). The Fe^{2+} content of the melt is calculated using the calibration of Kress and Carmichael (1991). The line through the data corresponds to a slope of 1.16, defined by the reversed experiments of Roeder and Reynolds (1991). Data from this study are consistent with that result.

between Rh, and to a lesser extend Ir, with the ferric iron content of spinels in lavas from Ambae volcano in the New Hebrides island arc. To show that the same is true for laboratory partitioning experiments, here we apply Eq. (10) in a somewhat more quantitative treatment of the global partitioning dataset for Ir and Rh in order to constrain estimates for k^{2+}_{tet} and k^{2+}_{oct}. In the context of divalent site occupancy, the most significant compositional variation in spinels amongst different PGE partitioning studies is the abundance of Fe^{3+}. We have therefore modeled the expected variation in Ir and Rh partitioning with ferric iron content using estimates of the cation site occupancy for binary Fe_3O_4–$FeCr_2O_4$. Chromite produced in this and previous studies also contain Mg–Al components, which may also affect the proportion of divalent coordination sites. However, the high temperature site occupancies are similar across the $MgAl_2O_4$–Fe_3O_4 join (Mattioli and Wood, 1988), so we expect that the spinel and magnetite components will have comparable effects on the divalent site occupancy in chromite. There is a decrease in the proportion of divalent VI-fold sites with the addition of the $FeAl_2O_4$ component to Fe_3O_4 (Nell et al., 1989), but this effect is minimized if we restrict our analysis to relatively Al-poor compositions (<25% of the trivalent cations) produced in this and previous studies.

Fig. 10A portrays the variation in D^{Ir}_{molar} with the $Fe^{3+}/(Fe^{3+}+Cr)$ of chromite for experiments done at 1850 °C and 2 GPa employing both graphite and Ir–Fe capsules (here and in subsequent plots, chromite compositions are projected on an Al-free basis to be consistent with the calculation of the inversion parameter for the Fe_3O_4–$FeCr_2O_4$ binary), along with results from low pressure experiments. For the experiments done at 2 GPa, there is a significant rise in the iridium partition coefficient with increased $Fe^{3+}/(Fe^{3+}+Cr)$, from a value of ~0.3 for the nearly Fe^{3+}-free composition, to ~20 at $Fe^{3+}/(Fe^{3+}+Cr)$ of 0.15. Although there are small differences in the Al content of these chromites, D-values are not correlated with $Al/(Fe^{3+}+Cr+Al)$ (not shown), indicating that the variation in Fe^{3+} exerts the dominant control on the change in inversion parameter. Superimposed on the data is the calculated variation in D^{Ir}_{molar} assuming the site occupancies for the Fe_3O_4–$FeCr_2O_4$ binary calculated at 1400 °C after the method of Kurepin (2005), and values for k^{2+}_{tet} and k^{2+}_{oct} of 0.9 and 1500, respectively (note that the temperature dependence of the site occupancies over the temperature range of the high and low pressure experiments is negligible). The value of k^{2+}_{tet} corresponds to that measured for chromite with the highest $Cr/(Fe^{3+}+Cr+Al)$ (experiment HTChr10). Whereas chromite from that experiment has no measurable Fe^{3+}, it does have $Al/(Fe^{3+}+Cr+Al)$ of 0.2, and likely some divalent octahedral sites. Hence, the estimated k^{2+}_{tet} is a maximum value. Although scatter exist in the experimental data, the theoretical curve reproduces the trend of the data reasonably well, providing validation for the model described above, and confirming the assumption of $k^{2+}_{tet} < k^{2+}_{oct}$. The values for D^{Ir}_{molar} measured by Righter et al. (2004) show significant variation, but are also consistent with the model. Fig. 10A also shows the empirically-determined D^{Ir}_{molar} reported by Pagé et al. (in press) using the composition of coexisting chromite and melt from the Alexo komatiite. Chromite compositions in this study were measured *in situ* by LA–ICP–MS, so the contribution of included platinum-group minerals (PGMs) is minimized. The empirical D^{Ir}_{molar} value of ~15 agrees with those we have measured, confirming that Ir is moderately compatible in ferric-iron poor chromite. This result contrasts with the value for D^{Ir}_{molar} of ~160 estimated by Puchtel and Humayen (2001) for chromite with similarly low Fe^{3+} from samples of the Vetreny komatiitic basalts. However, their empirical partition coefficient is based on chromite compositions measured by bulk analysis, which may have been subject to contamination by trace PGMs, or sulfide, as inferred for olivine-rich cumulates in a number of komatiite suites (e.g., Barnes and Fiorentini, 2008).

Model results for rhodium partitioning are shown in Fig. 10B. In this case the value for k^{2+}_{tet} of 0.24 is derived from the average of experiments HTChr 2 and 9 (chosen as per the iridium model),
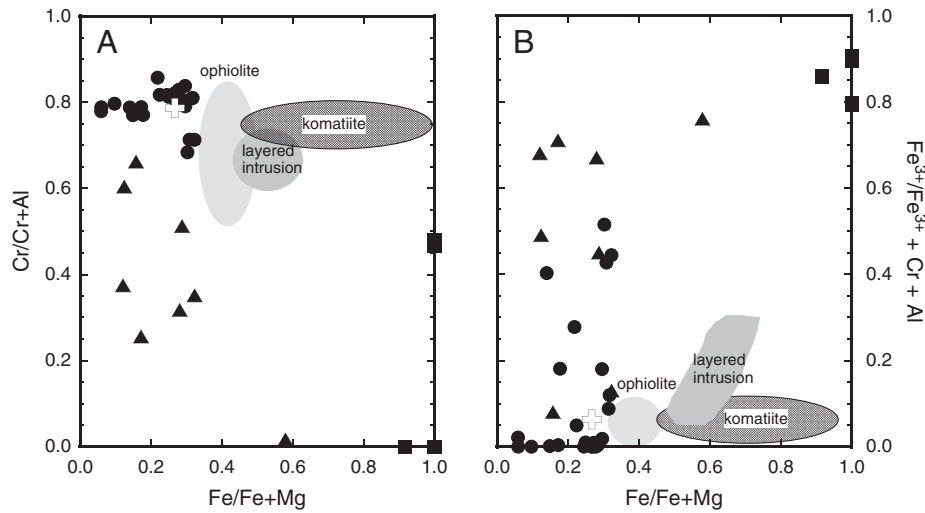
Fig. 5. Composition of spinel produced in this and past PGE partitioning experiments compared to those from select natural parageneses. Fields of spinel compositions from ophiolite, layered intrusions and komatiite correspond to the 90% density contour of Barnes and Roeder (2001). A) $Cr/(Cr + Al)$ as a function of $Fe^{2+}/(Fe^{2+} + Mg)$; B) $Fe^{3+}/(Fe^{3+} + Cr + Al)$ as a function of $Fe^{2+}/(Fe^{2+} + Mg)$. Note that the trend to high $Fe^{2+}/(Fe^{2+} + Mg)$ in some natural parageneses may represent subsolidus equilibration, particularly in the case of komatiites. Open cross: chromite starting material; filled circles: this study; filled triangles: Righter et al. (2004); filled squares: Capobianco et al. (1994).
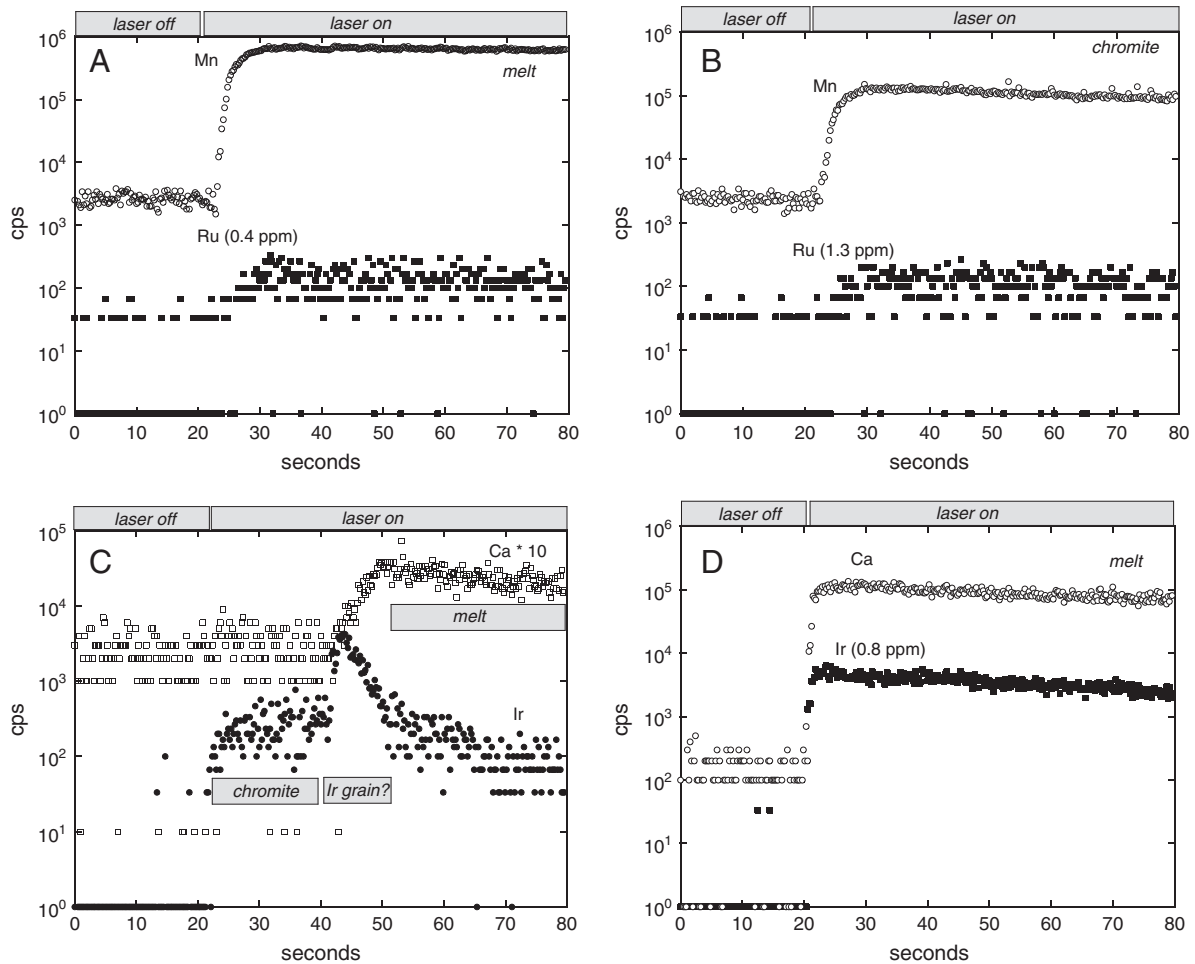
Fig. 6. Examples of time-resolved LA–ICP–MS spectra for quenched melts and chromite from partitioning experiments. Each spectra begins with 20 s of background collection with the laser off, then 60 s of sample ablation. A) Melt from experiment HTChr3. B) Chromite from HTChr3. Note the homogeneous distribution of Ru in both phases. C) Example of laser ablation through a small chromite crystal into melt from experiment HTChr39. The chromite–melt interface is designated by the sharp rise in the Ca signal. The prominent peak in the Ir signal originates in the melt near the chromite-glass interface, and infers the presence of an Ir-rich phase. D) Time-resolved spectra from the melt produced in experiment HTChr39. Note the homogeneity of the Ir signal, suggesting the absence of discrete Ir-rich phases.
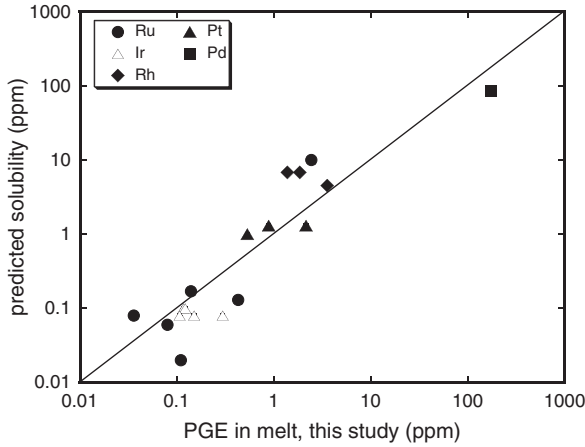
Fig. 7. Comparison between the PGE concentrations in melts produced in this study with previous solubility measurements at similar fO_2 and temperature. See Table 4 for results and the specific studies used for this comparison.

whereas the range for k^{2+}_{oct} was selected to reproduce the spread in magnetite–melt partitioning reported by Capobianco et al. (1994). Rhodium partition coefficients for spinel with intermediate ferric iron contents adhere well to the above partitioning model, and results from this study are best described by the curve for k^{2+}_{oct} of 750, which is at the low end of the magnetite data set. The origin of higher values for D^{Rh}_{molar} from other studies is not clear. Like iridium, the model for rhodium is also consistent with the assumption of $k^{2+}_{tet} < k^{2+}_{oct}$.

7.2. Ru partitioning: possible effects of melt speciation and electronic structure

Of the PGEs investigated in this study, ruthenium is clearly the most compatible in chromite, with measured D-values of ~4 (2 GPa, graphite encapsulated) to ~40 (0.1 MPa, gas mixing). As described above, this is consistent with Ru dissolving as a trivalent cation in oxide solutions at moderate to high fO_2 (Borisov and Nachtweyh, 1998), with a d^5 (low spin) electronic configuration in VI-fold coordination (Geschwind and Remeika, 1962), indicating a strong octahedral site preference. Like the
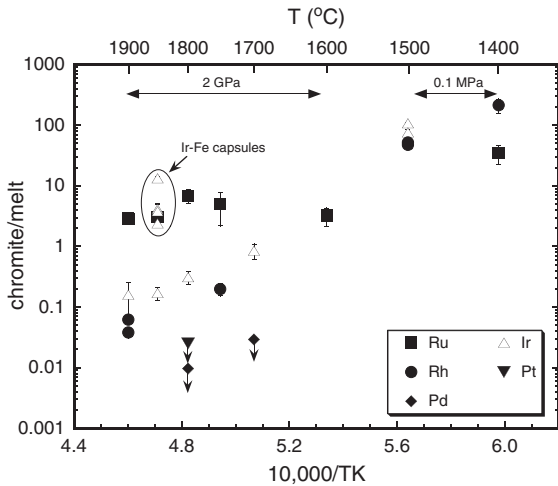
Fig. 8. Chromite–melt partition coefficient as a function of inverse absolute temperature, with °C portrayed on the top axis. Data points are labeled according to the element. Circled data correspond to Ir partitioning experiments done at 2 GPa using capsules made from Ir–Fe alloy. Experiments were done at T≥1600 °C, 2 GPa and 1400–1500 °C, 0.1 MPa.

divalent cations, the variation in partitioning behavior for trivalent cations should also adhere to relatively simple systematics based on IV- and VI-fold site occupancies in spinel. Analogous to the divalent case, the concentration of trivalent PGE cations in IV- or VI-coordination (c^{3+}_{tet} and c^{3+}_{oct}, respectively) is proportional to the abundance of each spinel site (y^{3+}_{tet} and y^{3+}_{oct}), the site affinities (k^{3+}_{tet} and k^{3+}_{oct}) and the total concentration of trivalent species in the melt (c^{3+}_{melt}). Derived in a manner analogous to the divalent case, the spinel–melt partition coefficient for trivalent cations can be written as:

$$C^{3+}_{tot,spinel} / c^{3+}_{melt} = \left(k^{3+}_{tet}\ y^{3+}_{tet}\right) + \left(k^{3+}_{oct}\ y^{3+}_{oct}\right) \qquad (11)$$

and given that y^{3+}_{tet} is equal to $x/3$ and $y^{3+}_{oct} = (2-x)/3$, the trivalent partition coefficient can be expressed on a molar basis as:

$$D^{3+}_{molar} = \left(k^{3+}_{tet}\ (x/3)\right) + \left(k^{3+}_{oct}\ ((2-x)/3)\right). \qquad (12)$$

In contrast to the divalent case, Eq. (12) predicts that the partition coefficient for trivalent cations should *decrease* with the degree of inversion, provided the cation affinity is larger for VI-fold, rather than IV-fold coordination. In the context of the described partitioning model, values of D_{Ru} should therefore decrease with an increase in the spinel Fe^{3+} content, since the proportion of trivalent VI-fold sites will be less. We estimate a value for $k^{3+}_{oct} = 11$ using the average of the chromite partitioning data, and assume a value for $k^{3+}_{tet} = 0.1$ (arbitrarily set as <1, but the result is relatively insensitive to this value, so long as $k^{3+}_{tet} < k^{3+}_{oct}$) to calculate a model partitioning curve from Eq. (12). Results are shown in Fig. 10C (curve A), along with Ru partitioning data from this and previous studies. Contrary to the model, the measured values for D_{Ru} are *larger* for spinels with higher $Fe^{3+}/(Fe^{3+} + Cr + Al)$, possibly because other species besides Ru^{3+} are involved in partitioning. In the derivation presented above, we implicitly assume that Ru predominantly exists as a trivalent species, but this may not be the case for the range of fO_2 investigated in this and previous studies. Specifically, at lower fO_2 the proportion of lower valence species, like Ru^{2+}, may increase, thus affecting the partitioning systematics. Therefore, the partition coefficient will be the sum of contributions from both species, and will vary with the degree of spinel inversion and species proportion, which both are functions of fO_2. Assuming that Ru^{2+} is the species present at more reduced conditions, analogous to the derivation above, the total concentration of Ru in spinel can be written as:

$$C^{Ru}_{spinel} = \left(k^{2+}_{tet}\ y^{2+}_{tet}\ C^{2+}_{melt} + k^{3+}_{tet}\ y^{3+}_{tet}\ C^{3+}_{melt}\right)$$
$$+ \left(k^{2+}_{oct}\ y^{2+}_{oct}\ C^{2+}_{melt} + k^{3+}_{oct}\ y^{3+}_{oct}\ C^{3+}_{melt}\right) \qquad (13)$$

and given that $y^{2+}_{tet} = (1-x)/3$, y^{3+}_{tet} and $y^{2+}_{oct} = x/3$ and $y^{3+}_{oct} = (2-x)/3$, the partition coefficient can be expressed on a molar basis as:

$$D^{Ru}_{molar} = \left[\left(\left(k^{2+}_{tet}\ ((1-x)/3)C^{2+}_{melt}\right) + \left(k^{3+}_{tet}\ (x/3)C^{3+}_{melt}\right)\right)\right.$$
$$\left. + \left(\left(k^{2+}_{oct}\ (x/3)C^{2+}_{melt}\right) + \left(k^{3+}_{oct}\ ((2-x)/3)C^{3+}_{melt}\right)\right)\right] / C^{Ru}_{melt} \qquad (14)$$

We have estimated the proportion of Ru^{2+} and Ru^{3+} as a function of fO_2 using the metal solubility data of Borisov and Nachtweyh (1998), with the details of this procedure provided in the Appendix. Model curve (B) shown in Fig. 10C is calculated according to Eq. (14), assuming the melt speciation determined from the Ru solubility data, and values of $k^{2+}_{tet} = k^{2+}_{oct} = k^{3+}_{tet} = 1$ and $k^{3+}_{oct} = 30$. The value for k^{3+}_{oct} dominates the form of the partitioning curve, as Ru^{3+} is the most
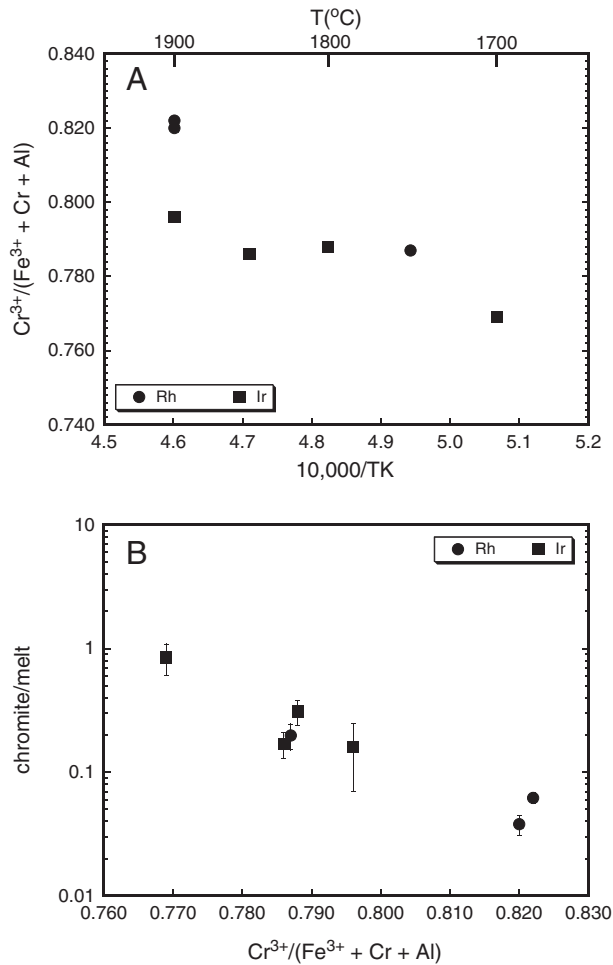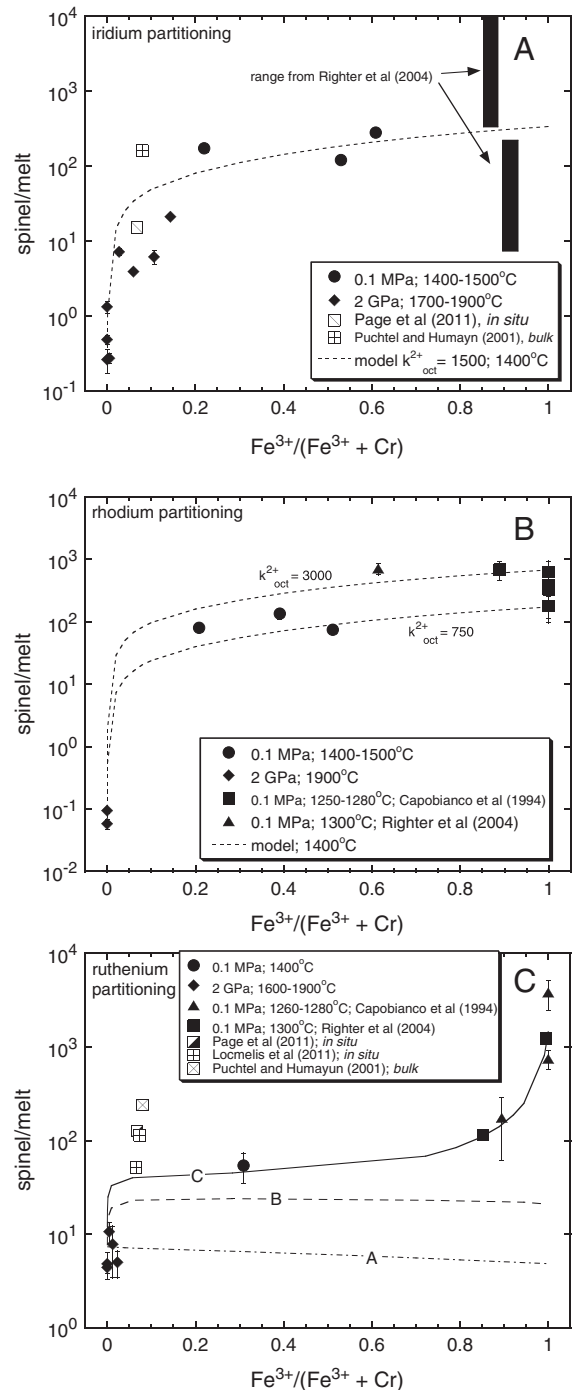
prevalent species, except at the relatively reduced conditions of our experiments. At these lower fO_2s, where Ru^{2+} becomes more abundant, the partition coefficient decreases, but only by the effect of a smaller C_{melt}^{3+} term in Eq. (14). Substitution of Ru^{2+} into spinel is negligible, as the proportion of divalent VI-fold sites is small for the Cr-rich compositions stable at these conditions. As such, changes of up to 1000-fold in the value of k for species in other sites has little effect on the form of the partitioning curve. Although the calculated curve reproduces the decrease in D_{Ru} for chromite-rich compositions, the magnitude of partition coefficients calculated for ferric iron-rich spinels is too low. Indeed, the partitioning model predicts a nearly constant value for D_{Ru} for more ferric-iron-rich compositions. Larger values of k_{oct}^{3+} result in partition coefficients for chromite that are too

Fig. 9. Results of experiments done to evaluate the effect of temperature on partitioning of Rh and Ir. A) $Cr/(Fe^{3+} + Cr + Al)$ in chromite as a function of inverse absolute temperature. Data show a decrease in this compositional parameter with decreasing temperature. B) Partition coefficient for Rh and Ir as a function of the $Cr/(Fe^{3+} + Cr + Al)$ in chromite. Results show that the partition coefficient falls with increasing amounts of Cr, consistent with a decrease in the availability of VI-fold sites to accommodate Ir^{2+} and Rh^{2+} cations. Thus, the change in the chromite–melt partition coefficient is consistent with the differences in the composition of chromite accompanying the variation in temperature.

Fig. 10. Variation in the spinel–melt partition coefficient across the chromite–magnetite join. In all cases spinels have $Al/(Fe^{3+} + Cr + Al) < 0.25$ so as to isolate the effect of Fe^{3+} on the spinel site occupancy. A) Data for Ir partitioning from experiments done at 0.1 and 2 GPa at the indicated temperatures. The vertical bars are the range of D-values determined from single experiments reported by Righter et al. (2004). Empirical determinations by Pagé et al. (in press) are based on *in situ* analyses of chromite by LA–ICP–MS, whereas those reported by Puchtel and Humayen (2001) are from analyses of chromite done by bulk methods. The dashed line is calculated from Eq. (10), assuming $k_{tet}^{2+} = 0.9$ and $k_{oct}^{2+} = 1500$, and values of the inversion parameter, x, calculated at 1400 °C after the method of Kurepin (2005). B) Comparison between measured and model values for rhodium partitioning. Model curves were calculated at 1400 °C for k_{tet}^{2+} of 0.24 and values for k_{oct}^{2+} of 750 and 3000. C) Comparison between measured and model values for ruthenium. Model curve "A" is calculated according to Eq. (12), and assumes Ru^{3+} is the only species, with constant values for k_{oct}^{3+} of 7 and $k_{tet}^{3+} = 0.1$. Model curve "B" is calculated according to Eq. (14), and assumes both Ru^{3+} and Ru^{2+} species, whose abundance varies according to Eq. (A1). The model uses constant values for k_{oct}^{3+} of 30 and $k_{tet}^{3+} = k_{tet}^{2+} = k_{oct}^{2+} = 1$. Model curve "C" is calculated according to Eq. (14), assuming the Ru speciation as per curve "B", but k_{oct}^{3+} which varies with chromite composition according to Eq. (A3). The model uses constant values of $k_{tet}^{3+} = k_{tet}^{2+} = k_{oct}^{2+} = 1$. Empirical measurements reported by Pagé et al. (in press) and Locmelis et al. (2011) are based on *in situ* LA–ICP–MS analyses of chromite, whereas values determined by Puchtel and Humayen (2001) used bulk chromite analyses.

high, and values for k_{tet}^{3+} which are $\gg 1$ result in a partitioning function that is concave down, and counter to the form of the data.

A plausible explanation for the much higher values for D_{Ru} in the more ferric-iron-rich spinels is that there is a mineral composition dependence to the partition coefficient. This suggestion is consistent with the results of Capobianco et al. (1994) who produced magnetite crystals in which increased Cr was correlated with decreased Ru abundance. Whereas the Ru concentration in those experiments was buffered by saturation in Ru metal, the Cr content of the melt diminished over the course of crystallization, hence implying a decrease in the compatibility of Ru with increased Cr substitution in magnetite. Based on trends in ionic radius with charge, we estimate that Ru^{3+} in VI-fold coordination should have an ionic radius of ~68 pm, similar to Fe^{3+} (64.5 pm) and somewhat larger than Cr^{3+} (61.5 pm). Therefore, the ionic radii of all three cations is rather similar, so the elastic strain contribution to the partitioning energetics will likely be small (Blundy and Wood, 1994). In contrast, the competition between Ru^{3+}, and either Fe^{3+} or Cr^{3+} for trivalent octahedral sites, could influence D_{Ru}. Whereas the OSPE for Cr^{3+} is the largest measured for transition metal cations, the OSPE for ferric iron in high spin state is zero or positive (Dunitz and Orgel, 1957; McClure, 1957; Navrotsky and Kleppa, 1967). We are not aware of any measurements of the OSPE for Ru^{3+}, but assume it to be similar to the isoelectronic Co^{3+}, and therefore approximately ½ that of Cr^{3+} (McClure, 1957). Consequently, the compositional dependence of Ru partitioning can be rationalized in terms of the relative stability gained by substitution of Ru^{3+} for the dominant trivalent cation in VI-fold coordination, which is largest for Fe^{3+}, and least for Cr^{3+}. We estimate the compositional dependence of k_{oct}^{3+} empirically by assuming that D_{Ru} for ferric-iron rich compositions is dominated by k_{oct}^{3+}, and that the most abundant Ru species over the fO_2 range of those experiments is Ru^{3+} (see the Appendix for details). We can therefore express k_{oct}^{3+} in terms of the modeled value of D_{molar}^{Ru} by the relation:

$$k_{oct}^{3+} \sim D_{molar}^{Ru} / ((2-x) / 3). \qquad (15)$$

Curve C in Fig. 10C is calculated from Eq. (14) assuming a compositional dependence for k_{oct}^{3+} determined in this manner. Although much of the calculated variation in D_{Ru} is derived from the empirical determination of k_{oct}^{3+}, and lacks thermodynamic rigor, the result does illuminate some important controls on spinel–melt partitioning. The need for a compositional dependence to k_{oct}^{3+} highlights the role of crystal field effects on the incorporation of certain cations into spinel, particularly if large differences exist in the OSPE between the substituent and host cation. Although the data are admittedly sparse, the variation in D_{Ir} and D_{Rh} with $Cr/(Fe^{3+}+Cr)$ are reproduced with constant values of k_{oct}^{2+}, consistent with the relatively small difference in OSPE for Fe^{2+} and Fe^{3+} (~5 kcal/mol) in contrast to Fe^{3+} and Cr^{3+} (~25 kcal/mol; Navrotsky and Kleppa, 1967). Additionally, the change in valence state from 3^+ to 2^+ can serve to reduce D_{Ru} by decreasing the C_{melt}^{3+} term in Eq. (14). The Ru^{2+} species contributes little to the total Ru inventory of Cr-spinel, as the proportion of divalent VI-fold sites is negligible for Cr-rich compositions. Thus, a combination of crystal field effects and changes in melt speciation conspire to reduce the compatibility of Ru in chromite with decreased fO_2.

Empirically-determined values for D_{molar}^{Ru}, derived from either in situ (Locmelis et al., 2011; Pagé et al., in press), or bulk (Puchtel and Humayen, 2001) chromite analyses are also portrayed in Fig. 10C. D_{molar}^{Ru} values based on in situ chromite analyses range from ~50 to ~130, which are similar to, and 3× greater than, respectively, the predicted curve. Puchtel and Humayen (2001) reported D_{molar}^{Ru} of ~240, which is ~6× larger than predictions. Although the large values of D_{molar}^{Ru} reported by Puchtel and Humayen (2001) could arise from PGM contamination (as described above) the time-resolved signal for Ru in the chromites analyzed by Pagé et al. (in press) and Locmelis et

al. (2011) are remarkably uniform, indicating the measured Ru is intrinsic to the chromite. A notable difference in the composition of the chromites from the natural samples characterized by in situ methods is the $Fe/(Fe+Mg)$ (Fe#), with the low value of D_{molar}^{Ru} corresponding to the chromites with Fe# of ~0.5 (Murphy Well komatiite), and the larger values for chromite with Fe# 0f ~0.35 (Alexo and Sullivans komatiite). Perhaps there is also a compositional dependence on Ru partitioning related to the dominant cation in IV-fold coordination at the fO_2 conditions at which Ru^{2+} is stable. More experiments which investigate this effect are clearly desirable.

7.3. Pt and Pd incompatibility in spinel

We put upper bounds on partition coefficients for Pt and Pd, with both values $\ll 1$. Metal solubility experiments have shown that Pt^{2+} and Pd^{1+} are the likely oxidation states at the fO_2 of our experiments (Borisov et al., 1994; Ertel et al., 1999). Pt^{2+} has a d^8 electronic configuration, and an ionic radius of 80 pm in VI-fold coordination (Shannon and Prewitt, 1970), similar to Fe^{2+} (78 pm), suggesting a strong preference for octahedral sites in the spinel structure. The relatively low value for D_{Pt} would therefore seem anomalous. However, we note that documented occurrences of VI-fold complexes containing Pt^{2+} are rare, with the square planar coordination being most common, stabilized by the enhanced bond strength overwhelming the pairing energy required for this configuration (Cotton and Wilkinson, 1988). Although square planar sites are unavailable in chromite, it may be that Pt^{2+} forms such complexes in the coexisting silicate melt, accounting for its preference for that phase. Alternatively, Brenan et al. (2003) suggested that the very low olivine–melt partition coefficients for Pt (<0.009) were more consistent with the prevalence of Pt^{4+} species, consistent with spectroscopic determinations (Farges et al., 1999). The ionic radii of Pt^{4+} and Ti^{4+} in VI-fold coordination are similar (63 and 60.5 pm, respectively; Shannon and Prewitt, 1969), with Pt^{4+} somewhat larger, predicting that D_{Pt} should be less than D_{Ti}. Calculated partition coefficients for Ti are ~0.2–0.3, compared to D_{Pt} of <0.03, which seems consistent with expectations. An accurate assessment of the behavior of Pt in these experiments awaits more information on the solution behavior of this element in molten silicate. Based on trends in size with charge (Shannon and Prewitt, 1969, 1970), Pd^{1+} is predicted to have an ionic radius of ~100 pm, so a combination of charge mismatch and elastic strain likely account for the exclusion of this cation from the chromite structure.

8. Summary and conclusions

Chromite–melt partitioning experiments have been done at high temperature, low fO_2 conditions designed to promote the solution of PGEs in the melt phase, but at the same time produce chromite with a low ferric iron content. Although D-values exhibit some variation with temperature, we show that such variations coincide with systematic changes in chromite composition, which we interpret as the overriding control on partitioning. Measured partition coefficients are considerably smaller than past experiments in which the ferric iron content of the spinel was high. We present a simple model which takes into account both the affinity of the PGE cation for a particular spinel lattice site, and the change in site occupancy across the chromite-magnetite join. Metal solubility experiments predict the predominance of divalent Rh and Ir over the range of fO_2 at which these and previous experiments have been done, and both cations have electronic configurations with a significant affinity for VI-fold coordination. Taking into account this information, we are able to model successfully the experimental data and show that the spinel–melt partition coefficient for Ir and Rh should rise rapidly with the ferric iron content of the spinel. Results suggest that D_{Ir} is ≤ 20 and D_{Rh} is ≤ 100 for ferric-iron poor, Cr-rich spinel compositions, the

phase that would crystallize in komatiites, some layered intrusions, and ophiolites.

Ru is found to be the most compatible in chromite of the PGEs investigated, which is consistent with the predominance of Ru^{3+} at experiment conditions and the similarity in the size of Ru^{3+} to Cr^{3+} and Fe^{3+}. Interpretation of the general increase in D_{Ru} with the ferric iron content of the spinel is not so straightforward, but likely involves a strong effect of mineral composition superimposed on a change in melt speciation (Ru^{3+} to Ru^{2+}) with fO_2. The effect of mineral composition probably stems from the difference in OSPE between Ru^{3+}, Fe^{3+} and Cr^{3+}, with larger partitioning into Fe^{3+}-rich compositions because of the enhanced reduction in energy gained by the Ru^{3+} substitution. Ru partition coefficients for ferric-iron poor spinel are predicted to be ~30, which is somewhat lower than values estimated from *in situ* analyses of natural chromite (Locmelis et al., 2011; Pagé et al., in press).

Experimental results and models indicate that the ferric iron content of chromite is an important compositional variable when assessing the compatibility of Rh, Ir and Ru. Future spinel–melt partitioning experiments of PGEs (and other transition metals) should therefore focus on ferric iron as a key parameter. Models of igneous differentiation should take into account the effect of Fe^{3+} when assessing the importance of spinel as a host for the PGEs. In reduced magmatic systems which crystallize Cr-rich, Fe^{3+}-poor chromite, it seems likely that PGM inclusions may better account for the association between chromite and the less compatible PGEs, like Ir, rather than their presence as a dissolved component (e.g., Barnes and Fiorentini, 2008). Both the measured and modeled chromite–melt partition coefficients for the PGEs are significantly less than values determined for sulfide melt–silicate melt partitioning (10^3 or greater), further confirming the strong control of accessory sulfide on whole-rock PGE budgets.

Appendix A

The amount of Ru^{2+} and Ru^{3+} at a given fO_2 was determined by fitting the Ru metal solubility data of Borisov and Nachtweyh (1998) to a function of the form:

$$\text{solubility (ppm)} = 10^{(0.5\Delta IW + a1)} + 10^{(0.75\Delta IW + a2)} \quad (A1)$$

in which a_1 and a_2 are solubility constants for the 2+ and 3+ valence states, respectively (determined to be −2.19 and −1.97; see O'Neill and Eggins, 2002 for details of this analysis). Although Borisov and Nachtweyh (1998) suggest that their data are consistent with Ru^{3+} as the sole species, the data are fit equally well with the two species model. Results indicate that Ru^{3+} is the dominant species over the fO_2 range at which the solubility measurements were made (IW + 6.8 to + 8.5), and predicts a crossover in relative species abundance at ~IW + 2.5 (Fig. A1), such that Ru^{2+} dominates at lower fO_2. There is likely some uncertainty in the exact position of the crossover point, however, owing to the effect of melt composition on cation speciation, as demonstrated for Mo (O'Neill and Eggins, 2002). Whereas Borisov and Nachtweyh (1998) used a diopside–anorthite eutectic composition, this and other partitioning studies have employed Fe-bearing "basaltic" compositions. Using the results for Mo as a guide, we expect that the uncertainty in the fO_2 of the crossover point is less than 2 log units, given that was the most extreme variation seen for melts of widely varying proportions of network-forming and network-modifying species. For the purposes of this discussion, it is sufficient that the crossover point exists at the fO_2 near that of our high pressure experiments.

In order to relate the Ru speciation to the composition of the spinel, a function describing the variation in spinel composition with fO_2 has to be determined. Ideally, this could be done using the same experiments used to measure Ru partitioning, but that work employed somewhat different bulk compositions, and involved variable doping levels of Cr. Instead, the relation between fO_2 and spinel composition across the chromite-magnetite join was determined using the experimental data of Horn et al. (1994). That study reports the composition of spinel grown in a synthetic alkali basalt composition at T = 1250–1300 °C at 1 bar over the fO_2 range of IW + 2 to + 10.3. Spinels produced in those experiments have nearly constant $Al/(Fe^{3+} + Cr + Al)$ of ~0.25, and compositions were normalized on an Al-free basis. We used the average composition taken from

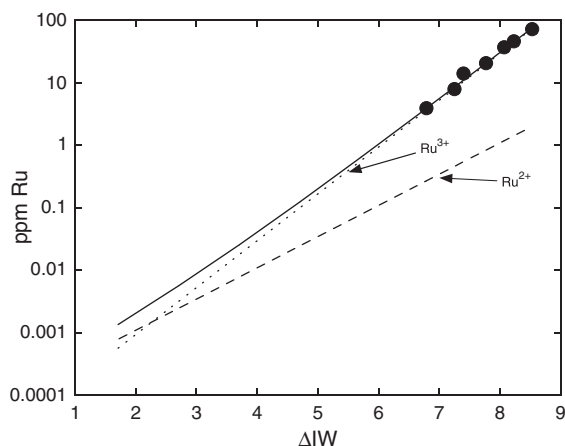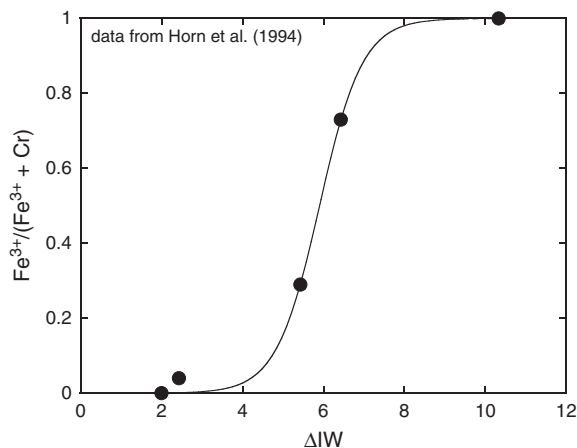**Fig. A1.** Measured and calculated solubility of Ru metal in silicate melt as a function of fO_2 relative to the IW buffer. Metal solubility was measured at 1400 °C using a Di-An eutectic melt composition (Borisov and Nachtweyh, 1998). The solid curve is determined by weighted least squares non-linear regression of the data according to Eq. (A1). The dashed curves correspond to the calculated concentration of the individual Ru species.

Fig. A2. Measured and calculated variation in the $Fe^{3+}/(Fe^{3+} + Cr)$ of spinel as a function of fO_2 relative to the IW buffer. Spinel compositions (calculated on an Al-free basis) are from Horn et al. (1994) and correspond to the average from multiple experiments done at 1250–1300 °C and the same relative fO_2. The curve is the fit to the data according to Eq. (A2).

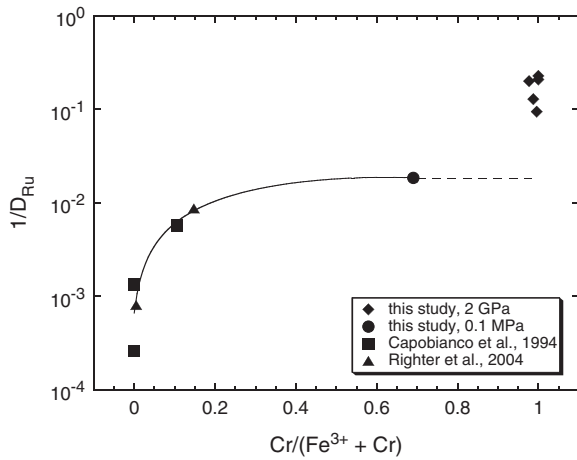**Fig. A3.** Plot of inverse D_{Ru} as a function of $Cr/(Fe^{3+}+Cr)$ in spinel to estimate the effect of spinel composition on k^{3+}_{oct}. For the compositional range of $0 < Cr/(Fe^{3+}+Cr) < 0.5$, the data are fit to a second order polynomial as per Eq. (A3) (see text for fit parameters). For more Cr-rich compositions, a constant value for $D_{Ru} = 60$ (dashed line) is used to calculate k^{3+}_{oct}. Values of $1/D_{Ru}$ for experiments done at 2 GPa in graphite capsules are offset from the experiments done at high fO_2, which we interpret as being the result of an increased proportion of the less compatible Ru^{2+}.

multiple experiments done at the same relative fO_2, which were then fit to a function similar to that used for Ru speciation:

$$X^{spinel}_{Fe_3O_4} = \left[10^{(m1*\Delta IW + n1)}\right] / \left[10^{(m1*\Delta IW + n1)} + 10^{(m2*\Delta IW + n2)}\right] \quad (A2)$$

which takes into account the change in iron speciation across this fO_2 range (Fig. A2). Regressed values for m1, n1, m2, n2 are 1.01, -3.36, 0.20 and 1.45, respectively. The model predicts the spinel to be pure chromite at conditions more reducing than $IW+2$, and pure magnetite at $IW+9$ and above.

The effect of spinel composition on the partition coefficient for Ru was estimated by fitting the data for magnetite-rich compositions obtained from experiments done in this study, those of Capobianco et al. (1994) and Righter et al. (2004). At the fO_2 at which those experiments were done, the predominant Ru species is Ru^{3+}, so the molar D_{Ru} has a simple relation to k^{3+}_{oct} (Eq. (15)). Inspection of the partitioning data suggests a function of the form:

$$1/D_{Ru} = a_0 + a_1 * \left\{Cr/\left(Fe^{3+}+Cr\right)\right\} + a_2 * \left\{Cr/\left(Fe^{3+}+Cr\right)\right\}^2 \quad (A3)$$

is appropriate (Fig. A3). Regressed values of the constants a_1, a_2 and a_3 are 6.65×10^{-4}, 0.058 and -0.047, respectively. Since D_{Ru} appears to level off for more Cr-rich compositions, we calculate values of k^{3+}_{oct} assume a limiting value for D_{Ru} of 60 for spinel with $Cr/(Fe^{3+}+Cr) > 0.5$.

References

Bacuta, G.C., Kay, R.W., Gibbs, A.K., Lipin, B.R., 1990. Platinum-group element abundance and distribution in chromite deposits of the Acoje block, Zambales ophiolite complex, Philippines. J. Geochem. Explor. 37, 113–145.
Ballhaus, C., Sylvestor, P., 2000. Noble metal enrichment processes in the Merensky Reef, Bushveld Complex. J. Petrol. 41, 545–561.
Barnes, S.J., Fiorentini, M.L., 2008. Iridium, ruthenium and rhodium in komatiites: evidence for iridium alloy saturation. Chem. Geol. 257, 44–58.
Barnes, S.J., Roeder, P.L., 2001. The range of spinel compositions in terrestrial mafic and ultramafic rocks. J. Petrol. 42, 2279–2302.
Blundy, J., Wood, B.J., 1994. Prediction of crystal–melt partition coefficients from elastic moduli. Nature 372, 452–454.
Borisov, A., Danyushevsky, L., 2011. The effect of silica contents on Pd, Pt and Rh solubilities in silicate melts: an experimental study. Eur. J. Mineral. 23 XXX-XXX.

Borisov, A., Nachtweyh, K., 1998. Ru solubility in silicate melts: experimental results in oxidizing region. Lunar Planet. Sci. XXIX, Abstract No. 1320.
Borisov, A., Palme, H., 1995. The solubility of iridium in silicate melts: new data from experiments with $Ir_{10}Pt_{90}$ alloys. Geochim. et. Cosmochim. Acta 57, 481–485.
Borisov, A., Palme, H., 2000. Solubility of noble metals in Fe-containing silicate melts as derived from experiments in Fe free systems. Am. Mineral. 85, 1665–1673.
Borisov, A., Palme, H., Spettel, B., 1994. Solubility of palladium in silicate melts: implications for core formation in the earth. Geochim. et. Cosmochim. Acta 58, 705–716.
Brenan, J.M., McDonough, W.F., 2009. Core formation and metal-silicate fractionation of osmium and iridium from gold. Nat. Geosci. 2, 798–801.
Brenan, J.M., McDonough, W.F., Dalpe, C., 2003. Experimental constraints on the partitioning of rhenium and some platinum-group elements between olivine and silicate melt. Earth Planet. Sci. Lett. 212, 135–150.
Brenan, J.M., McDonough, W.F., Ash, R., 2005. An experimental study of the solubility and partitioning of iridium and osmium between olivine and silicate melt. Earth Planet. Sci. Lett. 237, 855–872.
Brugmann, G.E., Arndt, N.T., Hofmann, A.W., Tobschall, H.J., 1987. Noble metal abundances in komatiite suites from Alexo, Ontario, and Gorgona Island. Colombia. Geochim. Cosmochim. Acta 51, 2159–2169.
Capobianco, C.H., Drake, M., 1990. Partitioning of ruthenium, rhodium, and palladium between spinel and silicate melt and implications for platinum-group element fractionation. Geochim. et. Cosmochim. Acta 54, 869–874.
Capobianco, C.H., Hervig, R.L., Drake, M., 1994. Experiments on crystal/liquid partitioning of Ru, Rh and Pd for magnetite and hematite solid solutions crystallised from silicate melt. Chem. Geol. 113, 23–43.
Cotton, F.A., Wilkinson, G., 1988. Advanced Inorganic Chemistry, 5th Ed .
Crocket, J.H., MacRae, W.E., 1986. Platinum-group element distribution in komatiitic and tholeiitic volcanic rocks from MunroTownship. Ontario. Econ. Geol. 81, 1242–1251.
Dunitz, J.D., Orgel, L.E., 1957. Electronic properties of transition metal oxides − II. Cation distribution amongst octahedral and tetrahedral sites. J. Phys. Chem. Solids 3, 318–323.
Eggins, S.M., Kinsley, L.P.J., Shelley, J.M.M., 1998. Deposition and element fractionation processes during atmospheric pressure laser sampling for analysis by ICPMS. Appl. Surf. Sci. 127–129, 278–286.
Ertel, W., O'Neill, H., St., C., Sylvester, P.J., Dingwell, D.B., 1999. Solubilities of Pt and Rh in haplobasaltic silicate melt at 1300 °C. Geochim. Cosmochim. Acta 63, 2439–2449.
Farges, F., Neuville, D.R., Brown, G.E., 1999. Structural investigation of platinum solubility in silicate glasses. Am. Mineral. 84, 1562–1568.
Ferraris, C., Lorand, J.-P., 2008. HRTEM-AEM-HAADF-STEM study of platinum-group elements within a mantle-derived Cr spinel (Lherz; North-Eastern Pyrenees, France). Earth Planet. Sci. Lett. 276, 167–174.
Finnigan, C.S., Brenan, J.M., Mungall, J.E., McDonough, W.F., 2008. Experiments and models bearing on the role of chromite as a collector of platinum group minerals by local reduction. J. Petrol. 49, 1647–1665.
Fiorentini, M.L., Beresford, S.W., Barley, M.E., 2008. Ruthenium–chromium variation: a new lithogeochemical tool in the exploration for komatiite-hosted Ni–Cu–(PGE) deposits. Econ. Geol. 103, 431–437.
Fortenfant, S.S., Gunther, D., Dingwell, D.B., Rubie, D.C., 2003. Temperature dependence of Pt and Rh solubilities in a haplobasaltic melt. Geochim. Cosmchim. Acta 67, 123–131.
Geschwind, S., Remeika, J.P., 1962. Spin resonance of transition metal ions in corundum. J. Appl. Phys. 33, 370–377.
Godel, B., Barnes, S.J., Maier, W.D., 2007. Platinum-group elements in sulphide minerals, platinum-group minerals, and whole-rocks of the Merensky Reef (Bushveld Complex, South Africa): implications for the formation of the reef. J. Petrol. 48, 1569–1604.
Hamlyn, P.R., Keays, R.R., Cameron, W.E., Crawford, A.J., Waldron, H.M., 1985. Precious metals in magnesian low-Ti lavas: implications for metallogenesis and sulfur saturation in primary magmas. Geochim. Cosmochim. Acta 49, 1797–1811.
Hart, S.R., Ravizza, G.E., 1996. Os partitioning between phases in lherzolite and basalt. Geophys. Monogr. 95, 123–134.
Hogg, A.J., Fawcett, J.J., Gittins, J., Gorton, M.P., 1989. Cyclical variation in composition in continental tholeiites of East Greenland. Can. J. Earth Sci. 26, 534–543.
Horn, I., Foley, S.F., Jackson, S.E., Jenner, G.A., 1994. Experimentally determined partitioning of high field strength- and selected transition elements between spinel and basaltic melt. Chem. Geol. 117, 193–218.
Hultgren, R., et al., 1973. Selected Values of the Thermodynamic Properties of Binary Alloys. American Society of Metals, New York, pp. 271–276.
Kress, V.C., Carmichael, I.S.E., 1991. The compressibility of silicate liquids containing Fe_2O_3 and the effect of composition, temperature, oxygen fugacity and pressure on their redox states. Contrib. Mineral. Petrol. 108, 82–92.
Kurepin, V.A., 2005. A thermodynamic model for Fe–Cr spinels. Contrib. Mineral. Petrol. 149, 591–599.
Laurenz, V., Fonseca, R.O.C., Ballhaus, C., Sylvester, P.J., 2010. Solubility of palladium in picritic melts: 1. The effect of iron. Geochim. Cosmochim. Acta 74, 2989–2998.
Legendre, O., Augé, T., 1986. Mineralogy of platinum-group mineral inclusions in chromitites from different ophiolite complexes. In: Gallagher, M.J., Ixer, R.A., Neary, C.R., Prichard, H.M. (Eds.), Metallogeny of Basic and Ultrabasic Rocks. Inst. Mining Metallurgy, London, U.K., pp. 361–375.
Locmelis, M., Pearson, N.J., Barnes, S.J., Fiorentini, M.L., 2011. Ruthenium in komatiitic chromite. Geochim. Cosmochim Acta 75, 3645–3661.
Lorand, J.P., Pattou, L., Gros, M., 1998. Fractionation of platinum-group elements and gold in the upper mantle: a detailed study in pyrenean orogenic lherzolites. J. Petrol. 40, 957–980.
Maier, W.D., Barnes, S.-J., 1999. Platinum-group elements in silicate rocks of the lower, critical and main zones at Union Section, Western Bushveld Complex. J. Petrol. 40, 1647–1671.

Mattioli, G., Wood, B.J., 1988. Magnetite activities across the MgAl$_2$O$_4$–Fe$_3$O$_4$ spinel join, with application to thermobarometric estimates of upper mantle oxygen fugacity. Contrib. Mineral. Petrol. 98, 148–162.

McClure, D.S., 1957. The distribution of transition metal cations in spinels. J. Phys. Chem. Solids 3, 311–317.

McLaren, C.H., DeVilliers, J.P.R., 1982. The platinum group chemistry and mineralogy of the UG2 chromitite layer of the Bushveld complex. Econ. Geol. 77, 1348–1366.

Mitchell, R.H., Keays, R.R., 1981. Abundance and distribution of gold, palladium and iridium in some spinel and garnet lherzolites: implications for the nature and origin of precious metal-rich intergranular components in the upper mantle. Geochim. et. Cosmochim. Acta 45, 2425–2442.

Morgan, J.W., Ganapathy, R., Higuchi, H., Krahenbiihl, U., 1976. Volatile and siderophile trace elements in anorthositic rocks from Fiskenaesset, West Greenland: comparison with lunar and meteoric analogues. Geochim. Cosmochim. Acta 40, 861–887.

Navrotsky, A., Kleppa, O.J., 1967. The thermodynamics of cation distributions in simple spinels. J. Inorg. Nucl. Chem. 29, 2701–2714.

Nell, J., Wood, B.J., Mason, T.O., 1989. High-temperature cation distributions in Fe$_3$O$_4$–MgAl$_2$O$_4$–MgFe$_2$O$_4$–FeAl$_2$O$_4$ spinels from thermopower and conductivity measurements. Am. Mineral. 74, 339–351.

O'Neill, H.St.C., Eggins, S.M., 2002. The effect of melt composition on trace element partitioning: an experimental investigation of the activities of FeO, NiO, CoO, MoO$_2$ and MoO$_3$ in silicate melts. Chem. Geol. 186, 151–181.

O'Neill, H.St.C., et al., 1995. Experimental petrochemistry of some high siderophile elements at high temperatures and some implications for core formation and the mantle's early history. Chem. Geol. 120, 255–273.

Page, N.J., von Gruenewaldt, G., Haffty, J., Aruscavage, P.J., 1982. Comparison of platinum, palladium, and rhodium distributions in some layered intrusions with special reference to the late differentiates (upper zone) of the Bushveld Complex, South Africa. Econ. Geol. 91, 439–450.

Pagé, P, Barnes, S-J., Bédard, J.H., Zientek, M.L., in press. In situ determination of Os, Ir, and Ru in chromites formed from komatiite, tholeiite and boninite magmas: implications for chromite control of Os, Ir and Ru during partial melting and crystal fractionation. Chemical Geology.

Park, J., Campbell, I.H., Eggins, S.M., 2010. The role of chromite crystallization on the PGE geochemistry of mafic magmas. : Misc. Release Data, 269. Ontario Geological Survey.

Peach, C.L., Mathez, E.A., 1996. Constraints on the formation of platinum-group element deposits in igneous rocks. Econ. Geol. 91, 439–450.

Peck, D.C., Keays, R.R., 1990. Insights into the behaviour of precious metals in primitive, S-undersaturated magmas: evidence from the Hazelwood River complex, Tasmania. Can. Mineral. 28, 553–577.

Peck, D.C., Keays, R.R., Ford, R.J., 1992. Direct crystallisation of refractory platinum-group element alloys from boninitic magmas: evidence from western Tasmania. Aust. J. Earth Sci. 39, 373–387.

Puchtel, I.S., Humayen, M., 2001. Platinum-group element fractionation in a komatiitic basalt lava lake. Geochim. et Cosmochim. Acta 65, 2979–2994.

Righter, K., Downs, R.T., 2001. The crystal structures of synthetic Re- and PGE-bearing magnesioferritespinels — implications for impacts, accretion and the mantle. Geophys. Res. Lett. 28, 619–622.

Righter, K., Campbell, A.J., Humayun, M., Hervig, R.L., 2004. Partitioning of Ru, Rh, Pd, Re, Ir and Au between Cr-bearing spinel, olivine, pyroxene and silicate melts. Geochim. et. Cosmochim. Acta 68, 867–880.

Roeder, P.L., Reynolds, I., 1991. Crystallisation of chromite and chromium solubility in basaltic melts. J. Petrol. 32, 909–934.

Shannon, R.D., Prewitt, C.T., 1969. Effective ionic radii in oxides and fluorides. Acta Cryst. B 25, 925–946.

Shannon, R.D., Prewitt, C.T., 1970. Revised values of effective ionic radii. Acta Cryst. 26, 1046–1048.

Talkington, R.W., Lipin, B.R., 1986. Platinum-group minerals in chromite seams of the Stillwater Complex, Montana. Econ. Geol. 81, 1179–1186.

Von Gruenewaldt, G., Merkle, R.K.W., 1995. Platinum-group element proportions in chromitites of the Bushveld complex: implications for fractionation and magma mixing models. J. Afr. Earth. Sci. 21, 615–632.

Walker, R.J., et al., 2008. Origin and chemical evolution of Group IVB iron meteorites. Geochim. et Cosmochim. Acta 72, 2198–2216.

Wißmann, S., Wurmb, V.V., Litterst, F.J., Dieckmann, R., Becker, K.D., 1998. The temperature-dependent cation distribution in magnetite. J. Phys. Chem. Solids 59, 321–330.

Yang, K., Thallhammer, O.A.R., Seccombe, P.K., 1995. Distribution of platinum-group elements in the great serpentinite belt of New South Wales, Eastern Australia. Mineral. Petrol. 54, 191–211.

Zhang, S.X., Wu, S.Y., Xu, P., Li, L.L., 2010. Theoretical investigations of the spin Hamiltonian parameters and the local structure for Rh^{2+} in rutile. Can. J. Phys. 88, 49–53.

Zhou, Mei-Fu, Min, Sun, Keays, R.R., Kerrich, R.W., 1998. Controls on platinum-group elemental distributions of podiform chromitites: a case study of high-Cr and high-Al chromitites from Chinese orogenic belts. Geochim. et. Cosmochim. Acta 62, 677–688.